AN ABSTRACT OF THE DISSERTATION OF

Landon Prisbrey for the degree of Doctor of Philosophy in Physics presented on October 13, 2011.

Title: Carbon Nanotube Devices Engineered by Atomic Force Microscopy

Abstract approved: _____

Ethan D. Minot

This dissertation explores the engineering of carbon nanotube electronic devices using atomic force microscopy (AFM) based techniques. A possible application for such devices is an electronic interface with individual biological molecules. This single molecule biosensing application is explored both experimentally and with computational modeling.

Scanning probe microscopy techniques, such as AFM, are ideal to study nanoscale electronics. These techniques employ a probe which is raster scanned above a sample while measuring probe-surface interactions as a function of position. In addition to topographical and electrostatic/magnetic surface characterization, the probe may also be used as a tool to manipulate and engineer at the nanoscale.

Nanoelectronic devices built from carbon nanotubes exhibit many exciting properties including one-dimensional electron transport. A natural consequence of one-dimensional transport is that a single perturbation along the conduction channel can have extremely large effects on the device's transport characteristics. This property may be exploited to produce electronic sensors with single-molecule resolution.

Here we use AFM-based engineering to fabricate atomic-sized transistors from carbon nanotube network devices. This is done through the incorporation of point defects into the carbon nanotube sidewall using voltage pulses from an AFM probe. We find that the incorporation of an oxidative defect leads to a variety of possible electrical signatures including sudden switching events, resonant scattering, and breaking of the symmetry between electron and hole transport. We discuss the relationship between these different

electronic signatures and the chemical structure/charge state of the defect. Tunneling through a defect-induced Coulomb barrier is modeled with numerical Verlet integration of Schrodinger's equation and compared with experimental results.

Atomic-sized transistors are ideal for single-molecule applications due to their sensitivity to electric fields with very small detection volumes. In this work we demonstrate these devices as single-molecule sensors to detect individual *N*-(3-Dimethylaminopropyl)-*N'*-ethylcarbodiimide (EDC) molecules in an aqueous environment. An exciting application of these sensors is to study individual macromolecules participating in biological reactions, or undergoing conformational change. However, it is unknown whether the associated electrostatic signals exceed detection limits. We report calculations which reveal that enzymatic processes, such as substrate binding and internal protein dynamics, are detectable at the single-molecule level using existing atomic-sized transistors.

Finally, we demonstrate the use of AFM-based engineering to control the function of nanoelectronic devices without creating a point defect in the sidewall of the nanotube. With a biased AFM probe we write charge patterns on a silicon dioxide surface in close proximity to a carbon nanotube device. The written charge induces image charges in the nearby electronics, and can modulate the Fermi level in a nanotube by ± 1 eV. We use this technique to induce a spatially controlled doping charge pattern in the conduction channel, and thereby reconfigure a field-effect transistor into a pn junction. Other simple charge patterns could be used to create other devices. The doping charge persists for days and can be erased and rewritten, offering a new tool for prototyping nanodevices and optimizing electrostatic doping profiles.

Carbon Nanotube Devices Engineered by Atomic Force Microscopy

by

Landon Prisbrey

A DISSERTATION

submitted to

Oregon State University

in partial fulfillment of
the requirements for the
degree of

Doctor of Philosophy

Presented October 13, 2011
Commencement June 2012

Doctor of Philosophy dissertation of Landon Prisbrey presented on October 13, 2011.

APPROVED:

_____

Major Professor, representing Physics

_____

Chair of the Department of Physics

_____

Dean of the Graduate School

I understand that my dissertation will become part of the permanent collection of Oregon State University libraries. My signature below authorizes release of my dissertation to any reader upon request.

_____

Landon Prisbrey, Author

ACKNOWLEDGEMENTS

CONTRIBUTION OF AUTHORS

Ji-Yong Park originally provided the idea to reconfigure nanoelectronic device function with charge nanolithography techniques in chapter 5. He also helped with interpretation and provided useful discussions in chapters 2 and 5. Tristan DeBorde performed the scanning photocurrent microscopy measurements and helped with interpretation in chapter 5. David Roundy performed numerical calculations and helped with interpretation in chapter 3. Kerstin Blank helped with single-molecule experiments in chapter 2, and provided interpretation and useful discussions in chapters 2 and 3. Leo Fifield helped with interpretation, and provided useful discussions in chapter 3. Guenter Schneider provided useful discussions in Chapter 4. Amir Moshar provided useful discussions in chapter 2.

Ethan Minot contributed to all aspects of this work, and co-authored all articles in this text.

TABLE OF CONTENTS

TABLE OF CONTENTS (Continued)

LIST OF FIGURES

LIST OF FIGURES (Continued)

LIST OF FIGURES (Continued)

LIST OF TABLES

To my parents.

My initiative evolved from their confidence in me.

To my lovely wife Kristina,

for her enduring support and patience.

PREFACE

I joined Ethan Minot's research group in Fall 2007 during my second academic year at Oregon State University. Initially I worked with Jörg Bochterle to fabricate quantum dots in a graphene sheet using scanning probe nanolithography techniques. We were unsuccessful in our task, but the electrical utilities we added to our group's atomic force microscope (AFM) I used constantly throughout the remainder of my research.

After this work I undertook an ambitious project, with a long term goal of using atomic-sized field-effect transistors for all-electronic detection of single enzyme activity. This work was largely motivated by recent progress by Brett Goldsmith in Phil Collins' group in UC Irvine. They had recently demonstrated single molecule sensing with such transistors. I began with computational simulations to verify that single enzymes would produce signals large enough to be detectable in such sensors. This work was published in the *Journal of Physical Chemistry B*.

In parallel to this theoretical project I began fabricating point-defect based carbon nanotube devices for use as single-molecule sensors. For this I learned a suite of semiconductor processing techniques to produce carbon nanotube network devices. In order to fabricate the atomic-sized transistor element from a network device I relied heavily on the work of Ji-Yong Park, who had pioneered scanning probe engineering of carbon nanotube devices.

The AFM-based characterization and engineering techniques I used to produce the atomic-sized transistors attracted the interest of Asylum Research. They invited us to author an application note on the subject to be included in their commercial AFM documentation. In writing this article I had the opportunity to work with Amir Moshar from Asylum Research. This work is additionally in press at *Microscopy and Analysis*.

Once I learned to fabricate atomic-sized transistors I began characterizing their transport properties and sought an explanation for the strange electronic behavior I observed. Eventually I developed a model, and Ethan Minot and David Roundy encouraged and aided me in refining it. This work is in review at the *Journal of Physical Chemistry C*.

In addition to understanding transport characteristics, I also attempted to use these devices for single-atom and single-molecule detection experiments. Mostly these experiments were unsuccessful; however, I believe we achieved single-molecule resolution on a few occasions. Our poor success rate is likely due to the lack of control of the chemical structure of the induced carbon nanotube defects.

During my last year of doctoral work I had the privilege to work closely with Ji-Yong Park from Ajou University (Korea), who was on sabbatical at Oregon State University. This was a special treat for me, since many of the engineering techniques I employed were based on his work. I learned a lot from him during his stay here. Quite on accident, I discovered an AFM technique to deposit surface charge on SiO_2 surfaces. This surface charge is retained for about a day under ambient conditions, and can be used as a 'side gate' to induce doping charge in nearby nanoelectronics. Dr. Park suggested that this charge could be used to spatially modulate the doping profile in a nanoelectronic device, thereby altering the function of the device. Together we published an article in *Applied Physics Letters* about reconfiguring the function of carbon nanotube devices with charge lithography.

In June 2011 Kerstin Blank, a collaborator from Radboud University (The Netherlands), visited for a series of experiments aimed at electronic single-molecule detection. We were able to witness interaction events between a diazonium salt (synthesized by Daniel Myles) and the carbon nanotube sidewall with single-molecule resolution. Soon we will author an article summarizing those experiments. In July I joined her group in Holland for further work towards electronic single-enzyme detection.

In addition to this work I participated in projects lead by other groups. In Walt Loveland's nuclear physics group I aided in high energy scattering experiments to determine fusion cross sections between heavy, neutron-rich, radioactive isotopes. I participated in experiments conducted at Oak Ridge National Lab in Tennessee, Argonne National Lab in Chicago, and TRIUMF national lab in British Columbia. These experiments lead to four publications. For Raghuveer Parthasarathy's biophysics group I aided in surface energy dissipation measurements of mycobacterial membranes in liquid using AFM. For Oksana Ostroverkhova's photonics and electronics group I provided electrostatic potential surface mapping to identify charge traps in thin film pentacene

transistors. For Christine Kelly's biotechnology group I provided liquid AFM surface distribution measurements of PEO-polybutadiene-PEO triblock surfactants to determine the brush layer morphology. I also provided AFM surface distribution measurements of beta-cyclodextrin labeled PBD backbones. For John Conley's materials science group I worked with Santosh Murali to investigate the function of memristive oxide nanoswitches using conductive AFM.

Landon Prisbrey
October 13th, 2011
Corvallis, Oregon

CHAPTER 1

Introduction

1.1 Introduction

In the last two decades the field of nanomaterials research has emerged. Its focus is on the creation, manipulation, and characterization of materials at nanometer length scales. Many materials, which are well understood in the bulk, exhibit suprising new properties when their dimensions are reduced to nanometer length scales. Nanomaterials research is centered on understanding this new behavior, which arises in the regime where classical and quantum physics overlap.

Through the application of nanomaterials, new technologies emerge with advantages over those based on bulk materials. Some promising applications include stronger materials,[1] disease targeting,[2] and faster and more energy efficient computer processors.[3] Many advantages arise simply from miniaturization, such as smaller electronic components,[4,5] more compact memory,[6,7] highly sensitive sensors,[8] and possibilities for in vivo pharmescuetical drug delivery systems.[9] Some of the most exciting applications are those which utilize quantum effects that are never exhibited in the bulk. For example, particles exhibit sharp optical resonances which are tunable as their dimensions are reduced to the nanometer length scales. The tunable fluorescence of such nanoparticle quantum dots is already used commercially in laser diodes,[10] and for tissue labeling.[11,12]

1.2 Scanning probe techniques

To study materials at nanometer length scales scientists have invented new tools. The first of these was the scanning tunneling microscope (STM).[13,14] The STM was invented in 1982 and was immediately recognized as an important revolution in materials science. Its inventors, Gerd Binnig and Heinrich Rohrer of IBM Zurich, were awarded the Nobel Prize in Physics only four years after its development. That same year they invented another breakthrough technology with Calvin Quate, the atomic force microsope (AFM).[15] These tools were a remarkable breakthrough which enabled researchers to study surfaces at previously unexplored length scales, and paved the way for nanomaterials research.

The AFM is utilized extensively throughout this work and what follows is a brief introduction. The AFM may be operated in a number of imaging modes, some provide topographical measurements, while others provide characterization of other surface properties. In many of these imaging modes the basic operation of the AFM is similar (Fig. 1.1). A laser is reflected from a cantilever containing a sharp probe (typical radius of curvature ~ 10 nm), and this reflected light is detected with a photodetector. In the case of topographical measurements the probe is brought into contact with the sample and then dragged along the surface while the deflection of the cantilever arm is measured as a change in the angle of the reflected laser light. A feedback loop utilizes this signal to adjust the vertical height of the probe, and in this way the surface topography can be mapped as a function of lateral tip position. Other imaging modes are variations on this theme, where probe-surface interactions are detected through a deflection of the cantilever.
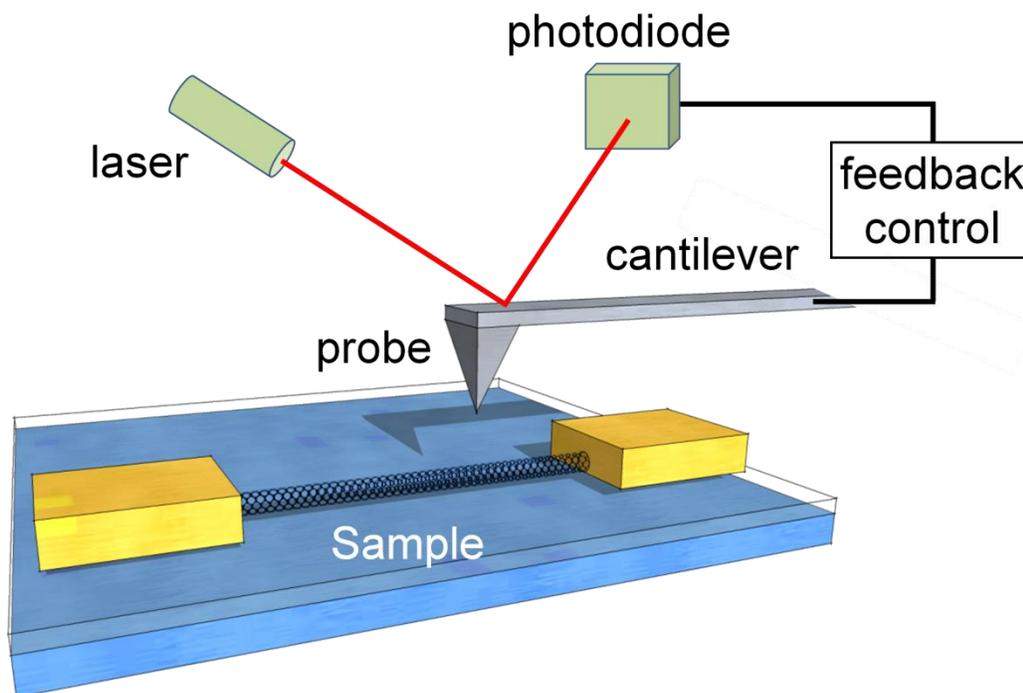
FIG. 1.1. Schematic of an atomic force microscope.

The advent of the AFM has made commonplace subnanometer topographical measurements, mostly commonly by dragging (see above) or tapping the tip along a

sample. However, many variations on this imaging scheme have been developed as researchers invent new AFM-based techniques for their own areas of research. These techniques allow for characterization of surface properties other than topography. For example, in the field of magnetic memory research, magnetized probes are used to map magnetization patterns,[16] while ferroelectric materials are studied by locating the electric fields from polarized domains.[17] In addition to characterization, the AFM is also used to manipulate matter at nanometer length scales.[18,19,20] It is possible, for example, to flip discrete magnetic or ferroelectric domains and then image the resulting changes,[17,21] or to construct a nanoscale electronic device by positioning nanoparticles between two electrodes with an AFM probe.[22] Chapter two of this thesis covers AFM-based techniques relevant to this work, which are used to study and engineer nanoelectronic devices (invited application note for *Asylum Research*, and in press at *Microscopy and Analysis,* 2012).[23]

1.3 Nanoelectronics

Nanoscale electronic devices are an area of intensive research. These devices offer many commercial possibilities due to optical transparency,[24] miniature size,[25] and low power consumption.[3] DNA sequencing, based on electronic detection of single protons, is already established by Life Technologies in a commercial setting.[26] In addition to engineering applications, nanoelectronic devices give researchers a powerful test bed for physical experimentation in the quantum realm. Exotic phenomena such as the Aharanov-Bohm effect,[27] zero mass particles,[28] the fractional quantum hall effect,[29] Luttinger-liquid behavior,[30] and single electron transport[20,31] have been observed.

Nanoelectronic devices have been made from graphene,[29] nanoparticles,[22] semiconducting nanowires,[32] and single molecules[33] including carbon nanotubes (CNTs).[34] CNTs are unique among this list in that they have the smallest cross section and largest aspect ratio.

Ever since their discovery[35] by Sumio Iijima in 1991 CNTs have been the focus of a great quantity of research. A CNT is a hollow tube of carbon atoms, arranged in a rolled up, chicken-wire structure (Fig 1.2). Diameters of single-walled CNTs range from 7 Å to

2 nm and can be grown up to millimeters long.[36] CNTs come in metallic and semiconducting varieties, and the small diameter and enormous aspect ratio lead to one-dimensional electron transport. Electronic devices built from CNTs were first demonstrated in 1997.[4,5]
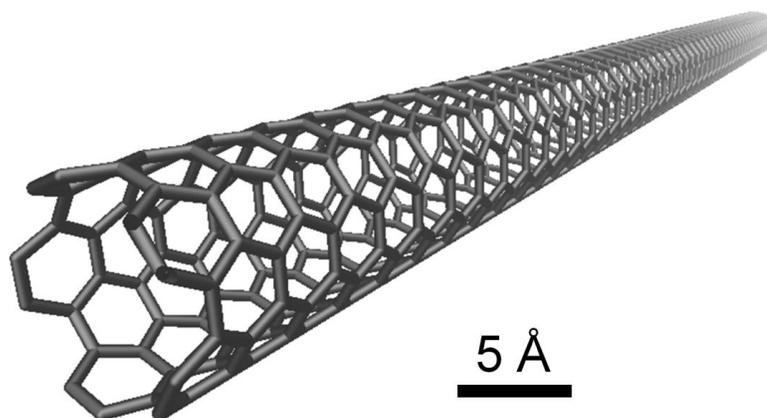
FIG. 1.2. A (5,5) carbon nanotube.

Often nanoscale devices are constructed in a field-effect transistor (FET) geometry. Figure 1.3 illustrates a CNT FET on a Si/SiO_2 substrate. A source-drain bias (V_{sd}) is applied across the CNT, and its Fermi level may be modulated via the back gate voltage (V_{bg}) connected to the doped silicon layer. The conductance of a FET device is dependent on the number of charge carriers in the conduction channel. As V_{bg} is changed, doping charge enters the channel and the conductance is modulated.
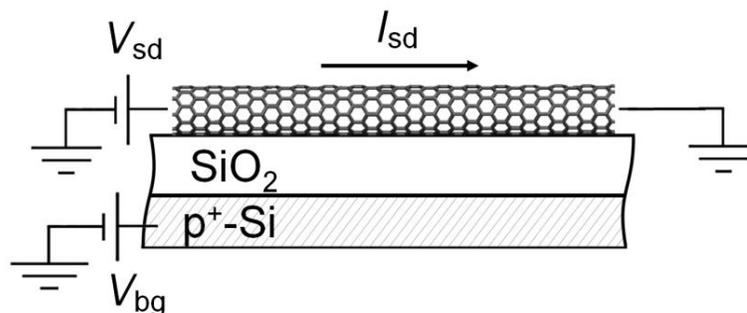
FIG. 1.3. Schematic illustrating a carbon nanotube field-effect transistor.

The function of a CNT FET device as shown in figure 1.3 can also be modified through the incorporation of a single point-defect in the CNT sidewall (Fig. 1.4). Point defects can be engineered into the CNT sidewall with voltage pulses from an AFM[37,38] or STM[39] probe, or through feedback-controlled chemical treatments.[40,41] A single defect can have a disproportionate effect on the device behavior because electronic transport through a CNT is one dimensional, and every charge carrier must travel through the defect. It has been shown that a CNT containing a single defect may function as a FET, where the field-effect response is localized to the region immediately surrounding the defect.[37,40] In these devices, the point defect acts as a bottleneck for electron transport, and the remainder of the CNT effectively behaves as contact electrodes to the atomic-sized transistor.
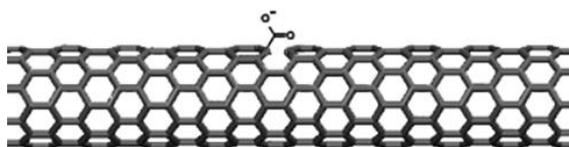
FIG. 1.4. A CNT with a carboxyl point defect.

These atomic-sized transistors approach the ultimate miniaturization limit, and offer many exciting possibilities due to their small size. They are attractive for miniaturization of integrated circuits, and for sensing applications at very small detection volumes. However, in order for these devices to find application there is still much work to be done to understand their fundamental properties. Existing techniques for engineering a point defect don't allow control of the chemical structure of the defect, and existing characterization techniques of defects remain crude. Work aimed toward engineering and characterization of defects is presented in chapter three. In that chapter we also attempt to resolve some of the inconsistancies between theory and experiment related to electronic transport though CNT defects (in review at *The Journal of Physical Chemistry C*).

1.4 Sensing Applications

As discussed above, the conductance of a FET device is modulated as a function of the electrostatic environment. In the example device illustrated in Figure 1.3, a global back gate used to control the electrostatic potential at the CNT, however, any source of electric field may be used to modulate the device conductance. For example, adsorbtion of charged molecules on the surface of the conduction channel can induce enough charge carriers in the device to cause a change in conductance.[42] A FET operating in this way is effectively a charge sensor, and intensive work is being applied to fashion selective sensors from nanoscale FETs for a wide range of sensing applications.[8,42,43,44]

Charge sensors built on these principles find many biological and medical applications, therefore, sensing experiments are often performed in an electrolyte solution meant to mimic physiological conditions (Fig. 1.5). In these environments mobile ions act to diminish electric fields over a characteristic length scale known as the Debye screening length, λ_D. This length effectively sets the detection volume of a CNT sensor operating in electrolyte (illustrated in Fig. 1.5)
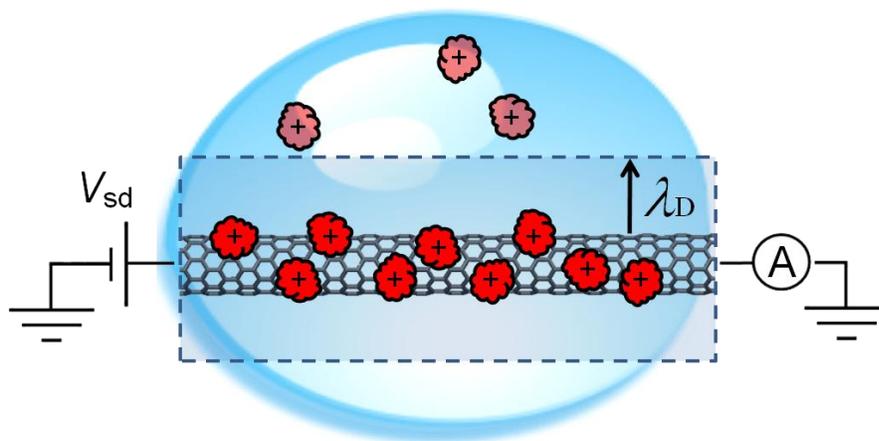
FIG. 1.5. A carbon nanotube sensor operating in an aqueous environment. The detection volume is a concentric cylinder around the CNT of radius λ_D (indicated by dashed line).

As discussed in section 1.3, an atomic-sized transistor device can be engineered from a CNT FET device through the incorporation of a single defect into the CNT sidewall (Figure 1.4). Due to the miniature size of the transistor element, point-defect based CNT sensors may be sensitive to electric fields at very small detection volumes (Fig. 1.6). Similar to the pristine CNT sensor described above (Fig. 1.5), the Debye screening length sets the effective detection volume in an electrolyte environment. However, instead of a cylindrical detection volume of radius λ_D (Fig. 1.4), the detection volume of an atomic-sized transistor is a sphere of radius λ_D. This suggests a dramatic reduction in detection volume compared to the pristine CNT device. Under physiological conditions this volume is on the order of 1 nm^3, allowing the possibility for sensor applications with single-molecule resolution.
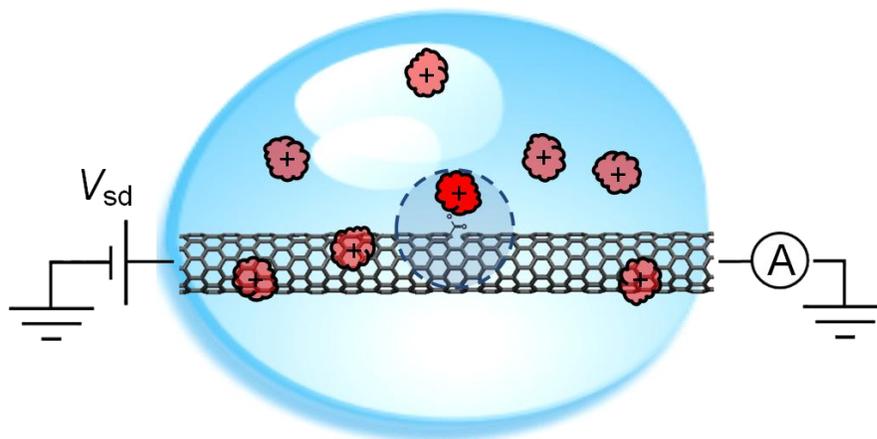
FIG. 1.6. A point-defect based sensor operating in an aqueous environment. The detection volume is a sphere of radius λ_D centered on the defect (indicated by dashed line).

Point-defect based CNT sensors have recently been used to study chemical reactions at the single-molecule level.[45,46] It has been suggested by Goldsmith, et al. that these sensors are ideal to study enzymatic activity at the single molecule level,[45] where

the defect acts both as the sensing element and as the anchor by which the enzyme is tethered to the device (Fig. 1.7).
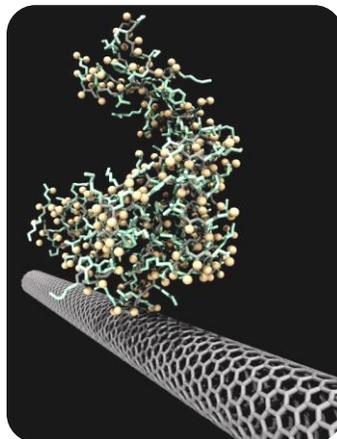
FIG. 1.7. The enzyme T4 Lysozyme tethered to a CNT point defect.

Studying enzymes at the single-molecule level reveals new phenomena which is lost in ensemble techniques such as nuclear magnetic resonance and activity assays. Single-molecule resolution reveals the time sequence of events for a single enzyme. This information can reveal the presence of active and unactive conformational states, transient intermediate states, and the presence of dynamic disorder in the catalytic activity. Currently, this information can be gained from molecular dynamics simulations[47] and fluorescence techniques.[47,48,49] However, these techniques have limitations. Simulations running on supercomputers are far from describing a single turnover event (~1 ms) because of the very short time step required. Single molecule fluorescence techniques have been around since 1990,[50] but remain challenging to implement and time intensive. As a result, to date there have only been a handful of enzymes which have been studied at the single molecule level.[49] Furthermore, fluorescence techniques suffer from other disadvantages. They require bulky fluorescent labels which potentially modify enzyme properties, and are typically limited to time scales of 1 ms to a few seconds.

Point-defect based CNT sensors offer a new and complementary approach to track single-enzyme activity. Accessible time scales are expected to be ~1 μs to hours,[51] and being charge sensitive, the technique is label-free. These attributes make point-defect based CNT sensors a complement to existing methods.

In an all-electronic detection scheme single-molecule processes are manifested as fluctuations in the conducatance of the transistor element. The simplest signals would originate from two state systems, where the reversible transition between the two states corresponds to a change in electrostatic potential at the transistor element. Figure 1.8 illustrates an example system which would produce this two-state telegraph signal. A protein is tethered to the atomic-sized transistor element, and the CNT carries a current I_{sd} (labeled (1) in Fig. 1.8) As the protein undergoes a conformational change, a charged region of the protein is moved closer to the CNT defect, thereby changing the electrostatic potential at the defect (labeled (2) in Fig. 1.8). The new local electrostatic potential induces a change in conductance, manifest as a reduction of current by ΔI. As the protein stochastically populates each conformation, a two-state fluctuation is observed in the conductance.
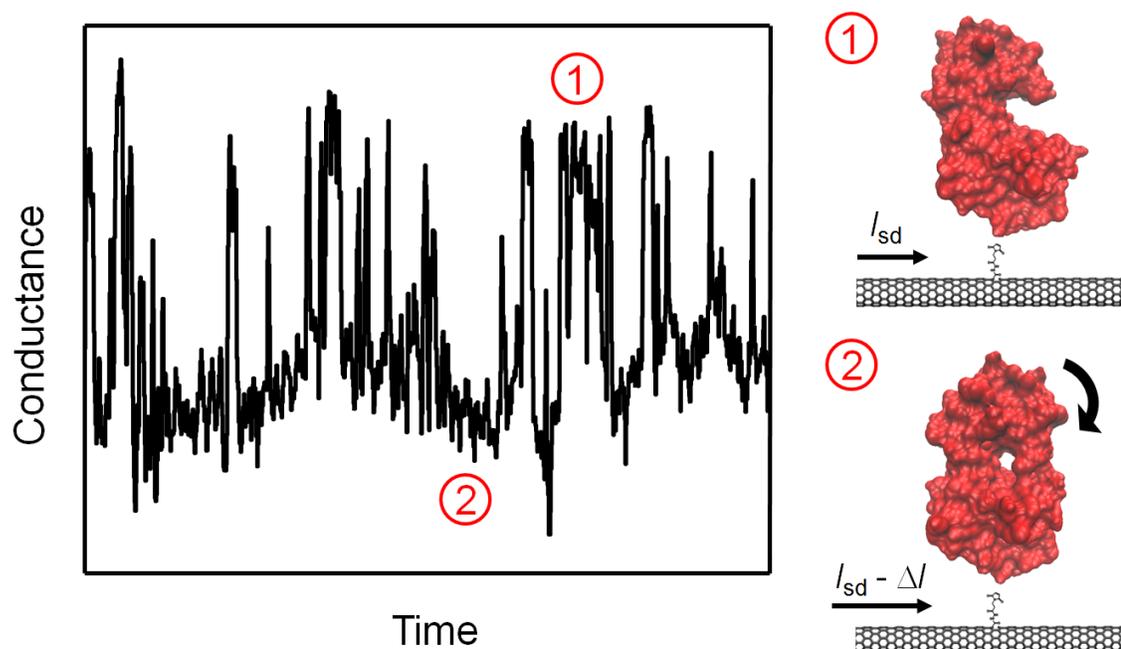
FIG. 1.8. Example signal expected from a single-molecule sensor. A two-state process (conformational change of a tethered protein) causes two-state telegraph noise in the conductance of the CNT.

In order to utilize nanoelectronics to study enzymes at the single-molecule level it must be ensured that signals generated from enzymatic activity can exceed device noise. In chapter four of this work we investigate this issue in a theoretical study of point-defect based CNT devices as single-enzyme sensors (published in *The Journal of Physical Chemistry B*, 2010).[51]

1.5 Other Applications

Nanoelectronic devices are not limited to only sensing applications. Often, the function of an electronic device is governed by the interface of two materials with different properties, such as a p-n junction or a metal-semiconductor junction. Control over the spatial doping profile in a FET device allows for modification of the function of the device. This can be achieved in a number of ways. For example, a nanoscale FET

device can be reconfigured into a pn junction through the use of a second gate electrode.[52] Devices in this geometery show great promise for solar energy conversion, and are a powerful test bed to explore fundamental optoelectronic properties of nanomaterials.[53,54] In chapter five of this thesis we demonstrate a new technique to control surface charge and therby the spatial doping profile in nanoelectronic devices. In this way, we alter the function of a nanoscale FET (published in *Applied Physics Letters*, 2011).[55] These techniques allow for on-the-fly device creation which may be used for prototyping nanoelectronic devices, and also find application in optoelectronics experiments.

References

1. Yu, M.-F. *et al.* Strength and Breaking Mechanism of Multiwalled Carbon Nanotubes Under Tensile Load. *Science* **287**, 637 -640 (2000).

2. Gao, X., Cui, Y., Levenson, R.M., Chung, L.W.K. & Nie, S. In vivo cancer targeting and imaging with semiconductor quantum dots. *Nat. Biotechnol* **22**, 969-976 (2004).

3. Xia, F., Mueller, T., Lin, Y.-ming, Valdes-Garcia, A. & Avouris, P. Ultrafast graphene photodetector. *Nat Nano* **4**, 839-843 (2009).

4. Tans, S.J. *et al.* Individual single-wall carbon nanotubes as quantum wires. *Nature* **386**, 474-477 (1997).

5. Bockrath, M. *et al.* Single-Electron Transport in Ropes of Carbon Nanotubes. *Science* **275**, 1922 -1925 (1997).

6. Fuhrer, M.S., Kim, B.M., Dürkop, T. & Brintlinger, T. High-Mobility Nanotube Transistor Memory. *Nano Letters* **2**, 755-759 (2002).

7. Radosavljević, M., Freitag, M., Thadani, K.V. & Johnson, A.T. Nonvolatile Molecular Memory Elements Based on Ambipolar Nanotube Field Effect Transistors. *Nano Letters* **2**, 761-764 (2002).

8. Zheng, G., Gao, X.P.A. & Lieber, C.M. Frequency Domain Detection of Biomolecules Using Silicon Nanowire Biosensors. *Nano Letters* **10**, 3179-3183 (2010).

9. Liu, Z., Sun, X., Nakayama-Ratchford, N. & Dai, H. Supramolecular Chemistry on Water-Soluble Carbon Nanotubes for Drug Loading and Delivery. *ACS Nano* **1**, 50-56 (2007).

10. Colvin, V.L., Schlamp, M.C. & Alivisatos, A.P. Light-emitting diodes made from cadmium selenide nanocrystals and a semiconducting polymer. *Nature* **370**, 354-357 (1994).

11. Chan, W.C.W. & Nie, S. Quantum Dot Bioconjugates for Ultrasensitive Nonisotopic Detection. *Science* **281**, 2016 -2018 (1998).

12. Bruchez, M., Moronne, M., Gin, P., Weiss, S. & Alivisatos, A.P. Semiconductor Nanocrystals as Fluorescent Biological Labels. *Science* **281**, 2013 -2016 (1998).

13. Binnig, G., Rohrer, H., Gerber, C. & Weibel, E. Tunneling through a controllable vacuum gap. *Applied Physics Letters* **40**, 178 (1982).

14. Binnig, G. & Rohrer, H. Scanning Tunneling Microscopy. *Surface Science* **126**, 236-244 (1983).

15. Binnig, G., Quate, C.F. & Gerber, C. Atomic Force Microscope. *Phys. Rev. Lett.* **56**, 930 (1986).

16. Parkin, S.S.P., Hayashi, M. & Thomas, L. Magnetic Domain-Wall Racetrack Memory. *Science* **320**, 190 -194 (2008).

17. Gruverman, A. Scanning force microscopy for the study of domain structure in ferroelectric thin films. *Journal of Vacuum Science & Technology B: Microelectronics and Nanometer Structures* **14**, 602 (1996).

18. Becker, R.S., Golovchenko, J.A. & Swartzentruber, B.S. Atomic-scale surface modifications using a tunnelling microscope. *Nature* **325**, 419-421 (1987).

19. Junno, T., Deppert, K., Montelius, L. & Samuelson, L. Controlled manipulation of nanoparticles with an atomic force microscope. *Applied Physics Letters* **66**, 3627 (1995).

20. Postma, H.W.C., Teepen, T., Yao, Z., Grifoni, M. & Dekker, C. Carbon Nanotube Single-Electron Transistors at Room Temperature. *Science* **293**, 76 -79 (2001).

21. Gibson, G.A., Smyth, J.F., Schultz, S. & Kern, D.P. Observation of the switching fields of individual Permalloyparticles in nanolithographic arrays via magnetic force microscopy. *IEEE Transactions on Magnetics* **27**, 5187-5189 (1991).

22. Junno, T. *et al.* Single-electron devices via controlled assembly of designed nanoparticles. *Microelectronic Engineering* **47**, 179-183 (1999).

23. Prisbrey, L., Park, J.-Y., Blank, K., Moshar, A. & Minot, E.D. Scanning probe techniques to engineer nanoelectronic devices. *Microscopy and Analysis* (2012).

24. Kim, K.S. *et al.* Large-scale pattern growth of graphene films for stretchable transparent electrodes. *Nature* **457**, 706-710 (2009).

25. Cui, Y. & Lieber, C.M. Functional Nanoscale Electronic Devices Assembled Using Silicon Nanowire Building Blocks. *Science* **291**, 851 -853 (2001).

26. Rothberg, J.M. *et al.* An integrated semiconductor device enabling non-optical genome sequencing. *Nature* **475**, 348-352 (2011).

27. Bachtold, A. *et al.* Aharonov-Bohm oscillations in carbon nanotubes. *Nature* **397**, 673-675 (1999).

28. Javey, A. & Kong, J. *Carbon Nanotube Electronics*. (Springer: 2009).

29. Zhang, Y., Tan, Y.-W., Stormer, H.L. & Kim, P. Experimental observation of the quantum Hall effect and Berry's phase in graphene. *Nature* **438**, 201-204 (2005).

30. Bockrath, M. *et al.* Luttinger-liquid behaviour in carbon nanotubes. *Nature* **397**, 598-601 (1999).

31. Roschier, L. *et al.* Single-electron transistor made of multiwalled carbon nanotube using scanning probe manipulation. *Applied Physics Letters* **75**, 728 (1999).

32. Björk, M.T. *et al.* Nanowire resonant tunneling diodes. *Applied Physics Letters* **81**, 4458 (2002).

33. Park, J. *et al.* Coulomb blockade and the Kondo effect in single-atom transistors. *Nature* **417**, 722-725 (2002).

34. Tans, S.J., Verschueren, A.R.M. & Dekker, C. Room-temperature transistor based on a single carbon nanotube. *Nature* **393**, 49-52 (1998).

35. Iijima, S. Helical microtubules of graphitic carbon. *Nature* **354**, 56-58 (1991).

36. Pan, Z.W. *et al.* Very long carbon nanotubes. *Nature* **394**, 631-632 (1998).

37. Park, J.-Y. Electrically tunable defects in metallic single-walled carbon nanotubes. *Appl. Phys. Lett.* **90**, 023112-3 (2007).

38. Park, J.-Y., Yaish, Y., Brink, M., Rosenblatt, S. & McEuen, P.L. Electrical cutting and nicking of carbon nanotubes using an atomic force microscope. *Appl. Phys. Lett.* **80**, 4446-4448 (2002).

39. Berthe, M. *et al.* Reversible Defect Engineering of Single-Walled Carbon Nanotubes Using Scanning Tunneling Microscopy. *Nano Letters* **7**, 3623-3627 (2007).

40. Goldsmith, B.R. *et al.* Conductance-Controlled Point Functionalization of Single-Walled Carbon Nanotubes. *Science* **315**, 77-81 (2007).

41. Coroneus, J.G. *et al.* Mechanism-Guided Improvements to the Single Molecule Oxidation of Carbon Nanotube Sidewalls. *ChemPhysChem* **9**, 1053-1056 (2008).

42. Li, J. *et al.* Carbon Nanotube Sensors for Gas and Organic Vapor Detection. *Nano Letters* **3**, 929-933 (2003).

43. Zheng, G., Patolsky, F., Cui, Y., Wang, W.U. & Lieber, C.M. Multiplexed electrical detection of cancer markers with nanowire sensor arrays. *Nat Biotech* **23**, 1294-1301 (2005).

44. Patolsky, F. *et al.* Electrical detection of single viruses. *Proceedings of the National Academy of Sciences of the United States of America* **101**, 14017 -14022 (2004).

45. Goldsmith, B.R., Coroneus, J.G., Kane, A.A., Weiss, G.A. & Collins, P.G. Monitoring Single-Molecule Reactivity on a Carbon Nanotube. *Nano Letters* **8**, 189-194 (2008).

46. Sorgenfrei, S. *et al.* Label-free single-molecule detection of DNA-hybridization kinetics with a carbon nanotube field-effect transistor. *Nat Nano* **6**, 126-132 (2011).

47. Henzler-Wildman, K.A. *et al.* Intrinsic motions along an enzymatic reaction trajectory. *Nature* **450**, 838-844 (2007).

48. Blank, K., Gert De Cremer & Johan Hofkens Fluorescence-based analysis of enzymes at the single-molecule level. *Biotechnology Journal* **4**, 465-479 (2009).

49. Blank, K., De Cremer, G. & Hofkens, J. Fluorescence-based analysis of enzymes at the single-molecule level. *Biotechnology Journal* **4**, 465-479 (2009).

50. Brooks Shera, E., Seitzinger, N.K., Davis, L.M., Keller, R.A. & Soper, S.A. Detection of single fluorescent molecules. *Chemical Physics Letters* **174**, 553-557 (1990).

51. Prisbrey, L., Schneider, G. & Minot, E. Modeling the Electrostatic Signature of Single Enzyme Activity. *The Journal of Physical Chemistry B* **114**, 3330-3333 (2010).

52. Lee, J.U. Photovoltaic effect in ideal carbon nanotube diodes. *Appl. Phys. Lett.* **87**, 073101 (2005).

53. Gabor, N.M., Zhong, Z., Bosnick, K., Park, J. & McEuen, P.L. Extremely Efficient Multiple Electron-Hole Pair Generation in Carbon Nanotube Photodiodes. *Science* **325**, 1367 -1371 (2009).

54. Gabor, N.M. *et al.* Hot Carrier-Assisted Intrinsic Photoresponse in Graphene. *arXiv:1108.3826* (2011).at <http://arxiv.org/abs/1108.3826>

55. Prisbrey, L., DeBorde, T., Park, J.-Y. & Minot, E.D. Controlling the function of carbon nanotube devices with re-writable charge patterns. *Appl. Phys. Lett.* **99**, 053125 (2011).

CHAPTER 2

Scanning probe techniques to engineer nanoelectronic devices

L. Prisbrey, J-Y. Park, K. Blank, A. Moshar, and E. D. Minot

A growing tool-kit of scanning probe microscopy-based techniques is enabling new ways to build and investigate nanoscale electronic devices. Here we review several advanced techniques to characterize and manipulate nanoelectronic devices using an atomic force microscope (AFM). Starting from a carbon nanotube (CNT) network device that is fabricated by conventional photolithography (micron-scale resolution) individual carbon nanotubes can be characterized, unwanted carbon nanotubes can be cut, and an atomic-sized transistor with single molecule detection capabilities can be created. These measurement and manipulation processes were performed with the MFP-3D AFM (Asylum Research) and illustrate the recent progress in AFM-based techniques for nanoelectronics research.

2.1 Author's note

The majority of the material contained in this chapter is published as an invited application note for *Asylum Research*, and has also been accepted for publication in *Microscopy and Analysis* (to be published April 2012). This chapter is a near duplication of those articles, but also contains additional material for added clarity and a more thorough exploration of the topic. These additions do not appear as an independent supplemental section. Instead, they have been inserted into the main line text of the original article to preserve the readability of the chapter. To examine the journal approved text, or to cite this work, we refer the reader to the forthcoming peer-reviewed publication.

2.2 Introduction

Research in nanoscale systems relies heavily on scanning probe microscopy. Many of these nanoscale systems have unique properties that are amenable to scanning probe techniques and, therefore, a wide variety of specialized scanning probe techniques have been developed. For example, in the field of magnetic memory research, magnetized probes are used to map magnetization patterns,[1] while ferroelectric materials are studied by locating the electric fields from polarized domains.[2] In many cases the

scanning probe microscope is used both as a manipulation tool as well as an imaging tool. It is possible, for example, to flip discrete magnetic or ferroelectric domains and then image the resulting changes.[2,3]

In the field of nanoelectronic devices, researchers have developed their own unique set of scanning probe imaging and manipulation techniques. In this article we review key techniques that allow for mapping the distribution of electrical resistances, measuring local field-effect sensitivity, and engineering new electrical characteristics into nanoscale devices. We use CNT devices as our working example, showing that CNTs in parallel can be analyzed, unwanted CNTs can be cut, and finally a point defect can be created which has single-molecule detection capabilities. While we focus on CNT devices, many of the same techniques are being used for nanowire[4] and graphene[5] devices.

2.3 Characterization modes

We first discuss how electric force microscopy (EFM) and scanning gate microscopy (SGM) techniques are used to characterize the electrical response of nanoelectronic devices. The information contained in EFM and SGM images is extremely valuable for relating the local electrical behavior of a device to the global device properties. In the specific example of our CNT network device, we use the knowledge of local resistance and local semiconducting behavior to choose the "best" CNT out of a mixture of parallel CNTs.
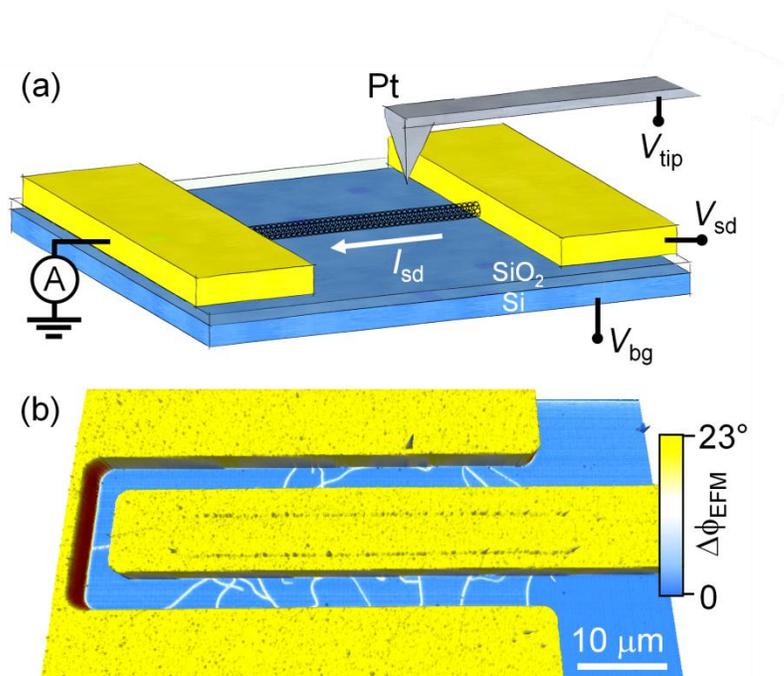
FIG. 2.1. (a) Schematic illustrating a carbon nanotube field-effect transistor and 'hover pass' (see text) microscopy geometries. Not to scale. (b) AFM topography colored with electric force microscopy phase ($V_{tip} = 8$ V, *height* = 20 nm).

To acquire EFM and SGM signals, a conducting AFM probe hovers above an electrically contacted device (Figure 2.1a). During a "hover pass", the microscope maintains a constant separation between the conductive AFM tip and the surface (typical separations are 20 - 200 nm). To achieve this constant separation distance, the microscope alternates between standard topographical line scans and hover pass line scans. A typical electrical contact configuration involves a current amplifier and three voltage sources (V_{sd}, V_{tip}, and V_{bg}). Depending on the particular imaging technique, different voltage signals will be applied and the AFM tip may or may not be piezoelectrically driven (see Table 2.1).

TABLE 2.1. Key differences between modes used for imaging nanoelectronic devices

	V_{sd}	Piezoelectrically driven?	'Hover Pass' Signal
dc-EFM	DC	yes	phase and amplitude
ac-EFM	AC @ $f_{cantilever}$	no	amplitude
SGM	DC	no	I_{sd}
tm-SGM	DC	yes	I_{sd}, AC @ $f_{cantilever}$

To demonstrate the utility of EFM and SGM, we used dc-EFM,[6] ac-EFM,[7] SGM,[8] and tip modulated SGM (tm-SGM)[9] to image a carbon nanotube (CNT) network device (Figures 2.1b and 2.2a). The device is fabricated by growing CNTs on a SiO_2/Si substrate (300 nm oxide),[10] and then patterning electrodes with photolithography. The images in Figures 2.1b and 2.2a are a combination of a dc-EFM data (color scale) and AFM topography. Many individual CNTs are seen bridging the gap between the source and drain electrodes. We are interested in learning which CNTs are metallic, which are semiconducting, which are well connected to the metal electrodes and which contain natural defects.
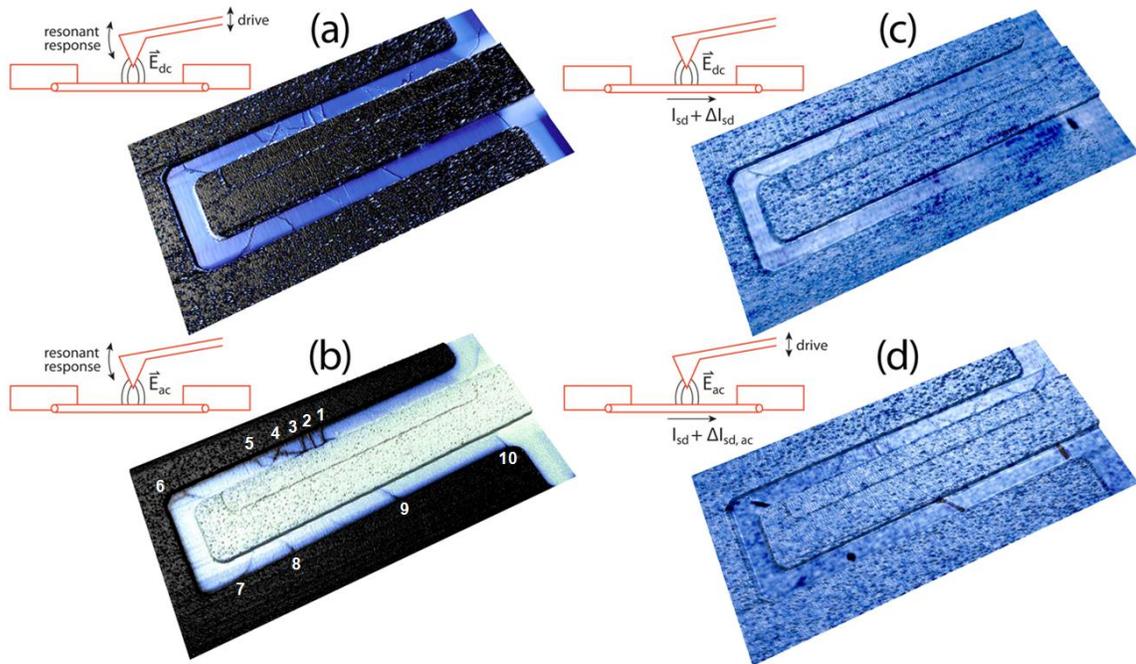
FIG. 2.2. 'Hover pass' microscopy data of a typical CNT FET. (a) Electric force microscopy (V_{sd} = 20 mV, V_{bg} = 0 V, V_{tip} = 5 V, *height* = 20 nm). Color scale shows phase of cantilever response. (b) Alternating current electric force microscopy (V_{sd} = 100 mV @ 63 kHz, V_{bg} = 0 V, V_{tip} = 2 V, *height* = 20 nm). Color scale shows amplitude of cantilever response. (c) Scanning gate microscopy (V_{sd} = 20 mV, V_{bg} = 0 V, V_{tip} = 5 V, *height* = 20 nm). Color scale shows the change in current, ΔI_{sd}, through the device. (d) Tip-modulated scanning gate microscopy (V_{sd} = 20 mV, V_{bg} = 0 V, V_{tip} = 5 V, *height* = 20 nm). Color scale shows the change in current at the cantilever fundamental frequency, $\Delta I_{sd,ac}$.

The electrostatic forces which give imaging contrast in dc-EFM[6] (Figure 2.1b and 2.2a) are due to a voltage difference between the tip and the grounded electrodes. During each hover pass, the AFM cantilever is piezoelectrically driven at a fixed frequency (the fundamental resonance of the cantilever). If the AFM tip is above a grounded conductor, a vertical gradient in electrostatic force causes a shift in the resonance frequency of the cantilever. This resonant frequency shift modulates both the phase and amplitude of the cantilever motion. The dc-EFM image shown in Figure 2.2a allows us to quickly locate all conducting objects in the large (60 μm) imaging area and requires minimal set-up.

The vertical gradient in electrostatic force, which gives rise to the dc-EFM signal, depends on the tip-sample capacitance and the tip-sample voltage difference. When the tip hovers above a large-area electrode, the vertical gradient in tip-sample capacitance is

large. When the tip hovers over a small CNT, the vertical gradient in tip-sample capacitance is small. Thus, the EFM signal from CNTs is weaker than from the electrodes. There has been steady progress in mapping out the vertical gradient in tip-sample capacitance to allow more quantitative imaging of the potential difference between the tip and the sample.[11,12]

Figure 2.2b shows an ac-EFM[7] image in which different voltage signals are sent to the source and drain electrodes, respectively. This type of ac-EFM scan is used to visualize the voltage profile along the length of electrically-biased CNTs. A similar measurement can be done with dc-EFM, however, the ac-EFM signal is cleaner (more discussion below). CNTs labeled 1-4 in Figure 2.2b exhibit a sharp voltage drop where they meet the inner electrode (the length of the CNT appears uniform black). This sudden voltage drop indicates a high contact resistance. The CNT labeled 5 exhibits a sharp voltage drop midway along its length. The location of the voltage drop corresponds to a sharp bend in the CNT, showing that the bend is a point of high resistance. CNTs labeled 6-10 show a gradual voltage gradient along their length, indicating that these CNTs are well connected to both electrodes, and are free from major electrical defects. These CNTs with small contact resistance will be subsequently singled out for additional engineering and experiments.

To obtain the ac-EFM signal in Figure 2.2b, an AC bias was applied to the outer electrode (frequency matching the cantilever's mechanical resonance) while the inner electrode and the AFM tip were grounded. During the hover pass the cantilever is not piezoelectrically driven, instead cantilever oscillations are driven by capacitive coupling to the AC biased electrode. These oscillations are detected by monitoring the cantilever deflection signal using a lock-in amplifier. The oscillation amplitude is plotted as a function of tip position to create the ac-EFM image. Cantilever oscillations are strongest when the probe is near the biased electrode. The ac-EFM signal is "cleaner" than dc-EFM signals because stray DC signals (such as charge on the insulating substrate) are invisible in ac-EFM.

We now turn our attention to scanning gate techniques, which allow researchers to further characterize the electronic properties of individual CNTs. Scanning gate

techniques identify the local semiconducting response of a nanoscale conductor, revealing the presence of localized semiconducting 'hotspots' and bottlenecks for electron transport.[8] Figure 2.2c shows an SGM image, where the AFM probe acts as a roaming gate electrode to modulate the doping in the underlying electronics. The SGM image (Figure 2.2c) shows a single feature, indicating that the global semiconductor response of the device is dominated by a single CNT (labeled 10 in Figure 2.2b). Other CNTs are present in the imaging area, but the SGM signals from these are significantly smaller. Methods to improve sensitivity are discussed below.

The imaging contrast in Figure 2.2c corresponds to changes in global device current when the biased probe locally changes the doping level in the underlying electronics. A small source-drain voltage (V_{sd}) is applied across the device to drive global current. By monitoring changes in current as a function of tip position, the local field-effect sensitivity can be mapped.

A variation of SGM which offers greater sensitivity is tip-modulated SGM (tm-SGM).[9] Compared to conventional SGM, tm-SGM offers higher spatial resolution and is capable of resolving weaker signals. Figure 2.2d shows a tm-SGM image. This scan reveals five CNTs with a semiconducting response (labeled 6-10 in Figure 2.2b). One CNT contains a region of highly localized semiconducting response, indicating the presence of a natural defect (labeled 8 in Figure 2.2b).

In tm-SGM the AFM cantilever is biased and piezoelectrically driven at its resonant frequency, resulting in an AC electric field which modulates the local doping level in the underlying electronics. The local field-effect response of the sample is mapped as a function of tip position by isolating the component of the conductance signal at the cantilever resonant frequency using a lock-in amplifier.

The detailed characterization outlined in Figure 2.2 allows us to pick the best CNT out of the ten CNTs for building a nanotransistor with chemical functionality. Using dc-EFM (Figure 2.2a), we identified the locations of all CNTs in a large area scan, providing a road map for engineering. With ac-EFM (Figure 2.2b) we identified desirable CNTs with low contact resistance (no sudden drop in voltage at metal-CNT contact) and an absence of natural defects (no sudden drop in voltage along length of CNT). Finally,

using SGM methods (Figures 2.2c and 2.2d), we identified CNTs with a semiconducting response. The most desirable CNT for building a nanotransistor is one with low contact resistance, no natural defects, and a uniform semiconducting response along its length. The CNT labeled 10 in Figure 2.2b satisfies these criteria, and is singled out for further experimentation.

2.4 Engineering modes

With initial characterization complete, we move to AFM manipulation techniques. Once a desired CNT is identified, we use AFM engineering to prune unwanted CNTs,[13] then engineer an atomic-sized transistor element into one remaining CNT.[14] These techniques combine AFM lithography modes with control of the tip-sample voltage. Mechanical manipulation by AFM has also been used by many authors,[15,16] but is not discussed here.

To cut unwanted CNTs, a Pt-coated AFM probe is biased to $V_{tip} = -10$ V, engaged with the surface, and then dragged through the CNTs in contact mode (contact force ~ 6-9 nN). Previously obtained dc-EFM and ac-EFM scans, such as in Figures 2.2a and 2.2b, provide a convenient road map of the locations of the unwanted CNTs. Figure 2.3 shows a time trace of global device conductance during electrical cutting. Sharp decreases in device conductance are observed as the CNTs are severed. Each cutting event produces a downward step in conductance with variable height. This variation reflects the fact that each nanotube has a unique electrical resistance. The vertical spike which appears following the second cut in figure 2.3b is due to the formation of a brief electrical connection between the negatively biased AFM probe and the sample electronics. After cutting, ac-EFM and SGM scans may be used to verify that a single CNT forms the only electrical contact between the electrodes.
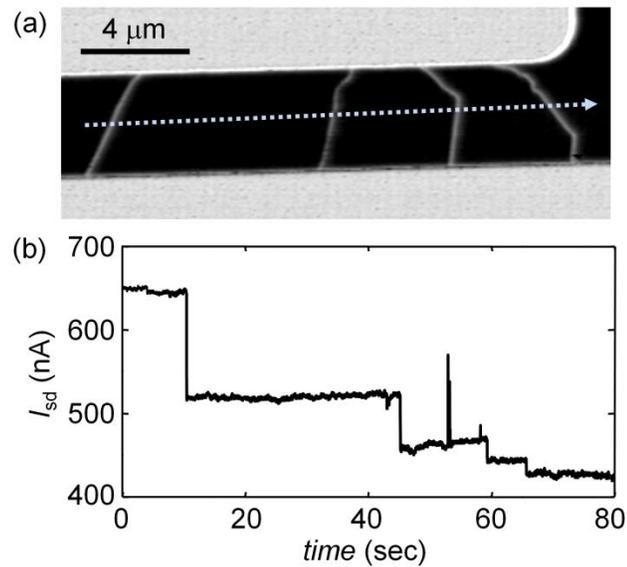
FIG. 2.3. Electrical cutting of unwanted CNTs. (a) Electric force microscopy image of a device. Cutting path indicated by dotted arrow (V_{sd} = 25 mV, V_{bg} = 0 V, V_{tip} = 8 V, *height* = 20 nm). (b) Time trace of cutting event (V_{sd} = 25 mV, V_{bg} = 0 V, V_{tip} = -8 V, *contact force* = 6-9 nN).

A single CNT can be converted into an atomic-sized transistor by further AFM-based engineering. Such nanotransistors approach the ultimate limit of miniaturization. To engineer an atomic-sized transistor, a conducting AFM probe is brought into gentle contact with the CNT and a -3 V, 15 ms square wave pulse is applied to the tip (Figure 2.4a). During the pulse, a chemical defect is incorporated into the sidewall of the CNT, and the device's electrical properties change significantly as a result (Figure 2.4b).[14,17] Typical defects add between 10 kΩ to 1 MΩ to the overall resistance of the circuit, and change the field-effect sensitivity of the device. Figure 2.4c shows a single-CNT device produced by the electrical 'nicking' method described above. SGM measurements show that the pristine CNT is uniformly gate sensitive (Figure 2.4d). Figure 2.4e shows an identical measurement following defect engineering, where gate sensitivity is localized to the region around the defect. The remainder of the CNT produces no signal due to its small resistance compared to the defect. The SGM scan reveals that the defect acts as a gate sensitive bottleneck for transport, and the remainder of the CNT serves only as contact electrodes to the miniature transistor.
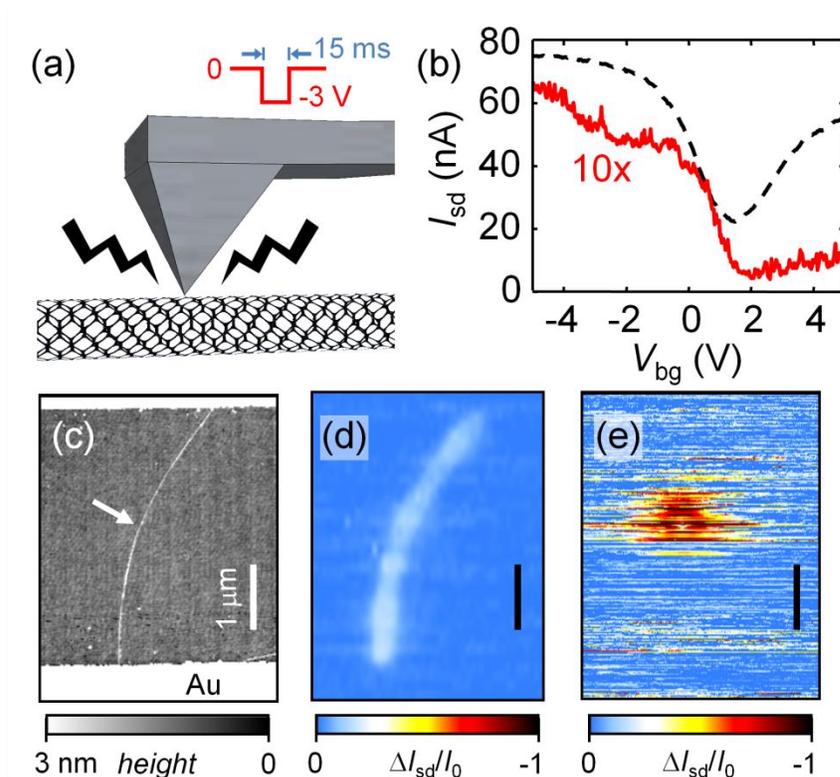
FIG. 2.4. Defect engineering in a CNT FET. (a) Schematic illustrating defect engineering geometry. (b) Transistor characteristics before (dashed black) and after (solid red) defect creation. The red curve has been multiplied by 10 (V_{sd} = 25 mV). (c) AFM topography of a CNT device. A defect was engineered at the location indicated by an arrow. (d) Scanning gate microscopy data of the device shown in (c) taken before and (e) after defect engineering (V_{sd} = 25 mV, V_{bg} = 0 V, V_{tip} = 8 V, *height* = 20 nm). The color scale ($\Delta I_{sd}/I_0$) indicates changes in device current relative to the baseline value, I_0. In (d) and (e) the values of I_0 are 280 nA and 7 nA, respectively.

A unique attribute of point-defect nanotransistors is their sensitivity to electrostatic potential within a very small detection volume. This attribute, combined with their high electrical resistance relative to the rest of the circuit, make them ideally suited for single-molecule sensing applications. Recently, point-defect nanotransistor sensors have been used to study biochemical reactions at the single molecule level.[18,19] Figure 2.5 demonstrates the use of an AFM-engineered point-defect nanotransistor as a single-molecule sensor. The reaction between *N*-(3-Dimethylaminopropyl)-*N′*-

ethylcarbodiimide (EDC) and a carboxyl group is used as a model reaction. EDC is frequently used to activate carboxyl groups in bioconjugation chemistry, and reacts reversibly with a carboxyl point defect on the CNT sidewall. The point-defect nanotransistor was immersed in an electrolyte solution containing EDC (Figure 2.5a). Figures 2.5b and 2.5c show the conductance data for a point-defect CNT before and after the addition of 20 μM EDC, respectively. Discrete switching events are observed in the presence of EDC. This two-state telegraph noise is believed to reflect changes in the electrostatic environment resulting from the reaction with single EDC molecules.[18] When EDC is bound to the defect, current through the CNT is low. When EDC releases from the defect, current through the CNT is high.
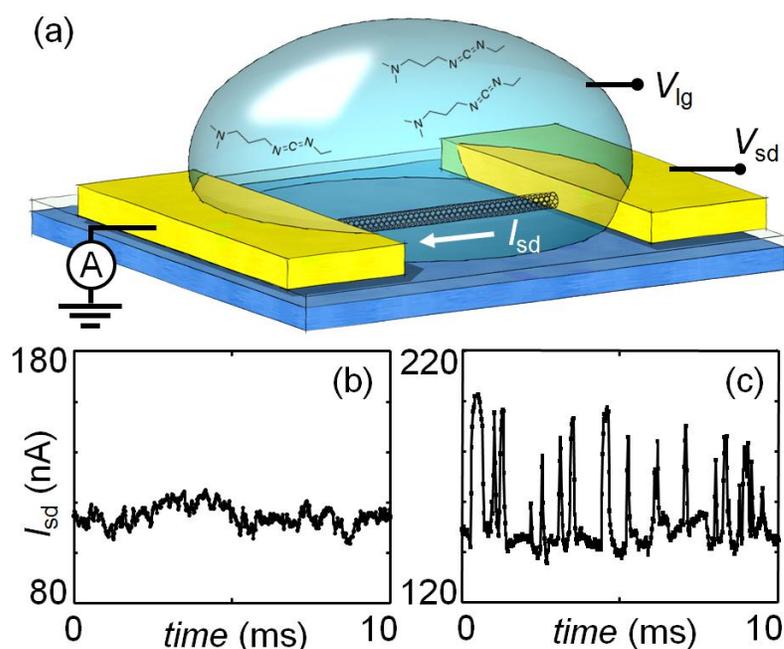
FIG. 2.5. Single-molecule detection of EDC. (a) Schematic illustrating detection geometry. The liquid potential is controlled with a liquid-gate electrode biased to V_{lg}. (b) I_{sd} trace of a nanotransistor in MES buffer (pH 4.5, V_{sd} = 25 mV, V_{lg} = 250 mV). (c) I_{sd} trace of the same device following the addition of 20 μM EDC (pH 4.5, V_{sd} = 25 mV, V_{lg} = 100 mV).

This two-state switching behavior is commonly attributed to a two state process, for example, binding and unbinding events. Illustrated in figure 2.6 are two possible configurations which could produce two-state switching. In the high conductance state

there are no EDC molecules within the detection volume of the sensor. When a molecule diffuses into the detection volume the device enters a low conduction state.

High conductance state

Detection volume

Current = I_{sd}

Low conductance state

Current = I_{sd} - ΔI_{sd}
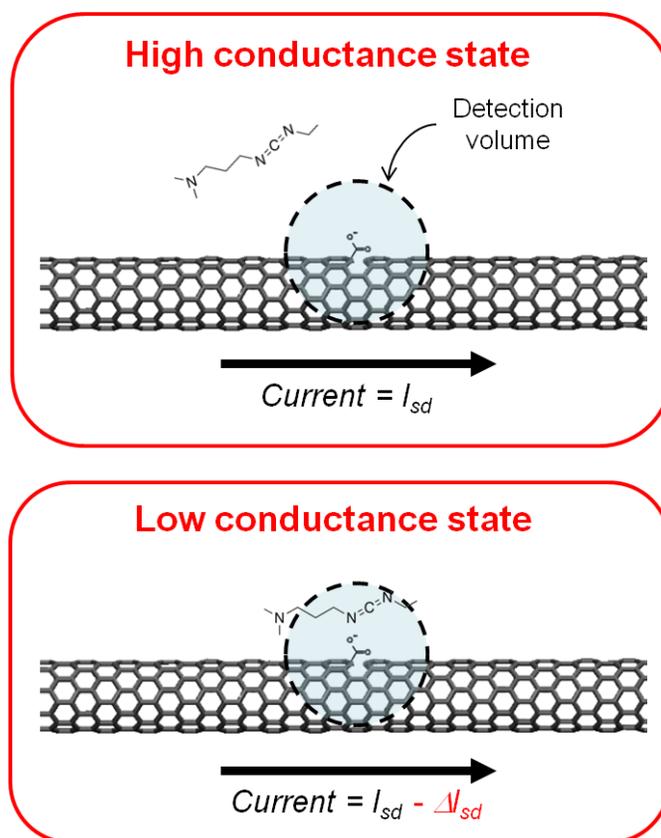
FIG. 2.6. Diagram illustrating a possible origin of the two-state switching signal.

2.5 Summary

Using CNT network sensors as our working example, we have reviewed AFM-based techniques which are used to study and engineer nanoelectronic devices. We have used dc-EFM and ac-EFM to identify the locations and resistances of individual CNTs that are electrically connected in parallel. Next, SGM and tm-SGM were used to reveal the semiconducting response of each CNT. With the information available in these scans a single CNT with desirable properties was singled out for further experimentation. The unwanted CNTs were electrically cut with a biased AFM probe to leave a device containing a single CNT. An atomic-sized transistor with chemical functionality was engineered in the remaining CNT using a voltage pulse from the AFM probe. This nanotransistor was then demonstrated to be a single molecule sensor sensitive to EDC in

an aqueous environment. This multi-step measurement and manipulation process illustrates the power of AFM-based techniques to map out and control the properties of nanoelectronic devices.

2.6 Acknowledgments

We thank Kristina Prisbrey for assistance with Figures 2.1, 2.4, and 2.5, and Bo Criss for assistance with Figure 2.2. We thank Sophie Ripp for initial experiments with EDC using suspended CNTs. We thank Paul Schuele and Sharp Labs of America for assistance with device fabrication. This work is funded by the Human Frontier Science Program. All AFM measurements and manipulation described here were performed with the MFP-3D AFM with the Probe Station Option (Figure 2.7, Asylum Research, Santa Barbara, CA, www.asylumresearch.com)
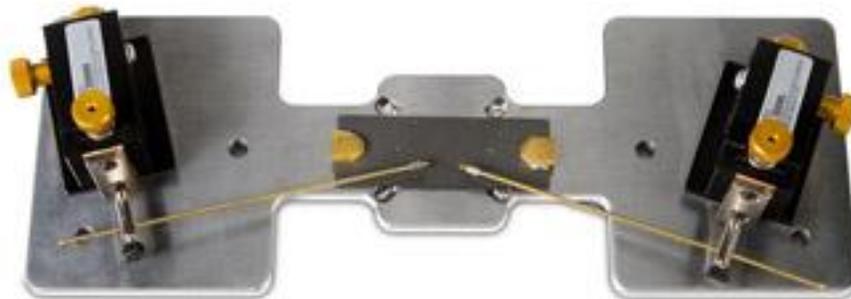
FIG. 2.7. The Probe Station attaches to the MFP-3D AFM scanner (Asylum Research, Santa Barbara, CA) and allows easy electrical probing of sample properties, electrical biasing, and other measurements while the sample is being scanned with the AFM. A variety of electrical connections can be made and combined with various imaging modes.

References and Notes

1. Parkin, S.S.P., Hayashi, M. & Thomas, L. Magnetic Domain-Wall Racetrack Memory. Science 320, 190 -194 (2008).

2. Gruverman, A. Scanning force microscopy for the study of domain structure in ferroelectric thin films. Journal of Vacuum Science & Technology B: Microelectronics and Nanometer Structures 14, 602 (1996).

3. Gibson, G.A., Smyth, J.F., Schultz, S. & Kern, D.P. Observation of the switching fields of individual Permalloyparticles in nanolithographic arrays via magnetic force microscopy. IEEE Transactions on Magnetics 27, 5187-5189 (1991).

4. Zhou, X., Dayeh, S.A., Wang, D. & Yu, E.T. Scanning gate microscopy of InAs nanowires. Applied Physics Letters 90, 233118 (2007).

5. Jalilian, R. et al. Scanning gate microscopy on graphene: charge inhomogeneity and extrinsic doping. Nanotechnology 22, 295705 (2011).

6. Martin, Y., Abraham, D.W. & Wickramasinghe, H.K. High-resolution capacitance measurement and potentiometry by force microscopy. Applied Physics Letters 52, 1103 (1988).

7. Bachtold, A. et al. Scanned Probe Microscopy of Electronic Transport in Carbon Nanotubes. Phys. Rev. Lett. 84, 6082 (2000).

8. Tans, S.J. & Dekker, C. Molecular transistors: Potential modulations along carbon nanotubes. Nature 404, 834-835 (2000).

9. Wilson, N.R. & Cobden, D.H. Tip-Modulation Scanned Gate Microscopy. Nano Letters 8, 2161-2165 (2008).

10. Kong, J., Soh, H.T., Cassell, A.M., Quate, C.F. & Dai, H. Synthesis of individual single-walled carbon nanotubes on patterned silicon wafers. Nature 395, 878-881 (1998).

11. Lei, C.H., Das, A., Elliott, M. & Macdonald, J.E. Quantitative electrostatic force microscopy-phase measurements. Nanotechnology 15, 627-634 (2004).

12. Yan, M. & Bernstein, G.H. A quantitative method for dual-pass electrostatic force microscopy phase measurements. Surface and Interface Analysis 39, 354-358 (2007).

13. Park, J.-Y., Yaish, Y., Brink, M., Rosenblatt, S. & McEuen, P.L. Electrical cutting and nicking of carbon nanotubes using an atomic force microscope. Appl. Phys. Lett. 80, 4446-4448 (2002).

14. Park, J.-Y. Electrically tunable defects in metallic single-walled carbon nanotubes. Appl. Phys. Lett. 90, 023112-3 (2007).

15. Junno, T., Deppert, K., Montelius, L. & Samuelson, L. Controlled manipulation of nanoparticles with an atomic force microscope. Applied Physics Letters 66, 3627 (1995).

16. Postma, H.W.C., Teepen, T., Yao, Z., Grifoni, M. & Dekker, C. Carbon Nanotube Single-Electron Transistors at Room Temperature. Science 293, 76 -79 (2001).

17. Kim, D.-H., Koo, J.-Y. & Kim, J.-J. Cutting of multiwalled carbon nanotubes by a negative voltage tip of an atomic force microscope: A possible mechanism. Phys. Rev. B 68, 113406 (2003).

18. Goldsmith, B.R., Coroneus, J.G., Kane, A.A., Weiss, G.A. & Collins, P.G. Monitoring Single-Molecule Reactivity on a Carbon Nanotube. Nano Letters 8, 189-194 (2008).

19. Sorgenfrei, S. et al. Label-free single-molecule detection of DNA-hybridization kinetics with a carbon nanotube field-effect transistor. Nat Nano 6, 126-132 (2011)

CHAPTER 3

Device characteristics of carbon nanotubes with engineered point defects

L. Prisbrey, D. Roundy, K. Blank, L. Fifield and E. D. Minot

A thorough understanding of how electrons pass through point defects in carbon nanotubes is crucial for building carbon nanotube devices. We have engineered point defects in the sidewalls of pristine carbon nanotubes via voltage pulses from a conducting atomic force microscope probe and studied the resulting changes in electron transport properties. We find that the incorporation of an oxidative defect leads to a variety of possible electrical signatures including sudden switching events, resonant scattering, and breaking of the symmetry between electron and hole transport. We discuss the relationship between these different electronic signatures and the chemical structure/charge state of the defect. Tunneling through a defect-induced Coulomb barrier is modeled with numerical Verlet integration of Schrodinger's equation and compared with experimental results.

3.1 Author's Note

The majority of the material contained in this chapter is under review at *The Journal of Physical Chemistry C*. This chapter is a near duplication of that article, but also contains additional material for added clarity and a more thorough exploration of the topic. These additions do not appear as an independent supplemental section. Instead, they have been inserted into the main line text of the original article to preserve the readability of the chapter. To examine the journal approved text, or to cite this work, we refer the reader to the forthcoming peer-reviewed publication.

3.2 Introduction

Recently much work has gone into utilizing the properties of defects in carbon nanotubes (CNTs). Devices with a single point defect have been used as single molecule sensors,[1,2] and CNT network devices with multiple defects have shown higher sensitivity to certain chemicals compared to pristine devices.[3]

It is an ongoing challenge to link theoretical and experimental studies of the electronic properties of CNT defects. Previous scanning tunneling microscope spectroscopy experiments have shown that defects can locally change the density of

states of a CNT.[4,5,6] Electron transport experiments on metallic CNTs with single defects have shown strongly suppressed conductance for electron doping, but much less suppression for hole doping.[1] Theoretical work has focused on band structure calculations of CNTs with defects, and often predicts the formation of localized impurity states in and around the band gap.[7,8,9,10,11,12,13] A small number of theoretical studies have attempted to link defect structure to electron transport characteristics.[7,14]

Oxidative defects in CNTs are typically introduced using gas phase or liquid phase treatments such as exposure to heat,[15] ozone,[16,17] acids,[1,18,19,20] or peroxides.[21,22] Depending on the oxidant and/or process, a variety of oxidative defects can be created in the sidewall of a CNT such as ethers/epoxides (C-O-C), alcohols (C-OH), ketones/aldehydes (C=O), and carboxylic acids (COOH).[23,24] Bulk chemistry using the above methods yields mixtures of these different oxidation states. To generate individual point defects for single molecule sensing, feedback-controlled electrochemical attack[1] and local anodic oxidation utilizing voltage pulses from an AFM[25,26] or STM[27] probe have been applied. None of these techniques offer control over the chemical nature of the defect, and only carboxylic acid groups have been previously identified at the single-defect level.[20]

We have used the AFM technique to create oxidative point defects in 15 different individually-contacted quasi-metallic CNTs (small band gap CNTs) and observed a variety of different transport signatures. Half of our stable post-defect devices showed strongly suppressed conductance for electron doping, but much less suppression for hole doping. We present a new model to explain this characteristic behavior. Other post-defect devices showed electron transport characteristics that are consistent with resonant scattering from impurity states, suggesting that a defect's impurity state spectra can be acquired through low-bias electrical measurements. Overall, our results illustrate the wide range of electron transport characteristics that are associated with oxidative point defects in CNTs and suggest new ways to identify the chemical structure of point defects.

3.3 Methods

Individual CNT devices were made by patterning iron catalyst on a SiO_2/Si substrate (300 nm oxide) and growing CNTs by catalyzed chemical vapor deposition.[28] Source and drain electrodes were patterned with photolithography to produce circuits with a number of CNTs connected in parallel. Electric force microscopy[29] and scanning gate microscopy (SGM)[30] were used to identify circuits whose gate response is dominated by a single CNT (Figure 3.1).
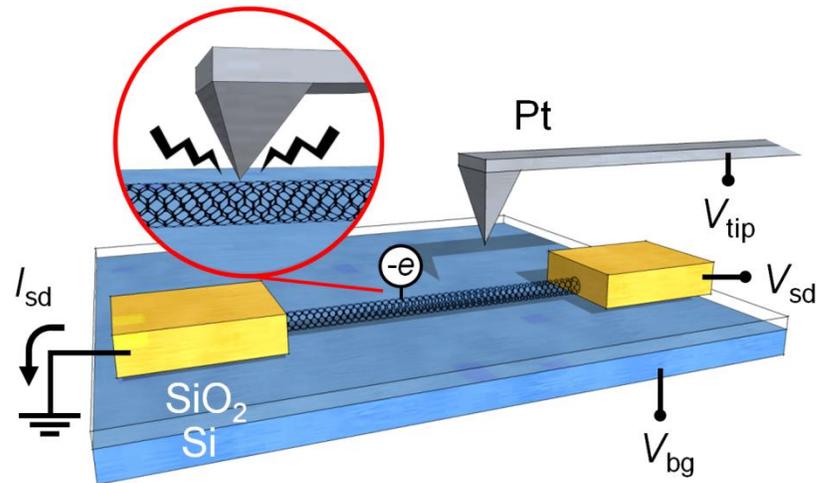
FIG. 3.1. Schematic illustrating CNT FET device, defect engineering, and scanning gate microscopy geometries. Not to scale.

Point defects were engineered in ambient conditions with voltage pulses from a Pt coated AFM probe.[25,26,31] A homebuilt AFM stage with electrical probes was used to contact the CNT device. A small source-drain bias (V_{sd} = 25 mV) was applied to monitor the conductance of the device before, during, and after modification. To engineer a defect we lower the AFM probe onto the CNT (*contact force* = 6 - 9 nN) and apply a -3 V, 15 ms square wave pulse to the tip.

3.4 Results and discussion

Successful defect engineering is manifested as a drop in CNT conductance. Afterward, the CNT may remain permanently modified or else 'self heal', which we observe as an abrupt return of the conductance to the pre-modified state.

We first discuss the self-healing phenomenon. Figure 3.2 shows electrical current through a CNT before, during, and after defect engineering (V_{sd} = 25 mV throughout the experiment). When a voltage pulse was applied from an AFM tip at t = 20 s, a sudden increase in resistance was observed (a drop in current). The device remained modified for 4 seconds before the resistance returned to the pre-modified state. We note that the self-healing event does not coincide with lifting the AFM tip away from the surface.
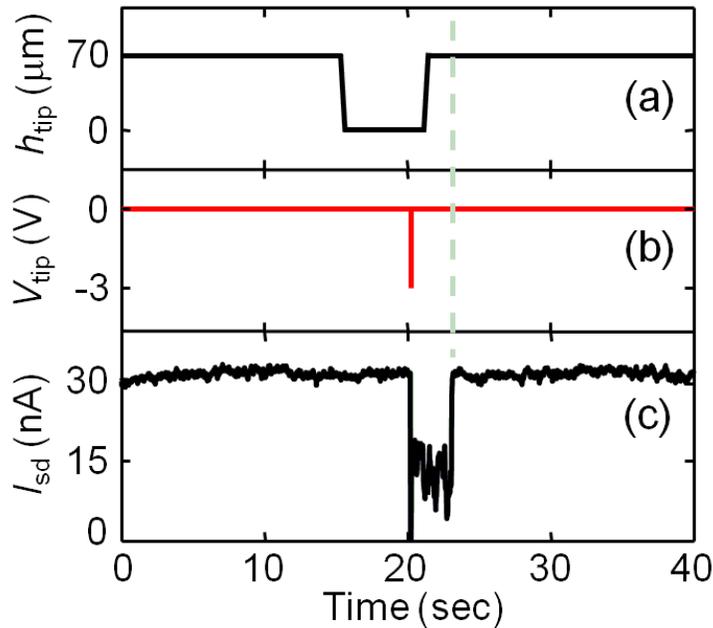
FIG. 3.2. The creation of a short-lived CNT defect. The tip was lowered until it touched the CNT, a voltage pulse was applied between the AFM tip and the CNT, and the tip was retracted. Shown are time traces of (a) tip height, h_{tip}, (b) tip voltage, V_{tip}, and (c) current through the CNT (V_{sd} = 25 mV).

It is reasonable to assume that a short-lived defect is chemically unstable and/or energetically unfavorable. For example, the following two mechanisms might be considered. The voltage pulse may lead to C-C bond rotation that is reversible with fast time scales at room temperature.[27] Alternatively, oxygen might be added to the nanotube in a high-energy configuration, leading to structural rearrangements and subsequent elimination of the oxygen.[7] Although not clearly defined chemically, our current results show that these unstable states can be observed by transport measurements at the single defect level.

Unstable defects are not relevant for the development of CNT electronics applications and we now focus on CNTs with oxidative defects that were long lived. Scanning gate microscopy measurements, where a biased AFM tip operates as a roaming local gate (Figure 3.1), were performed before and after stable defect engineering to confirm that electrical transport is dominated by the introduced defect. Shown in Fig. 3.3a is a topology scan of a pristine CNT. SGM measurements show that it is gate sensitive along its entire length (Figure 3.3b). An identical measurement following defect engineering reveals that gate sensitivity is localized to the region around the defect, and this region is behaving as a bottleneck for charge transport (Figure 3.3c). Control experiments show that the observed effects were not caused by local charge injection into the oxide.[32] Voltage pulses were applied between the AFM tip and the oxide near the CNT with no observable effect on conductance.
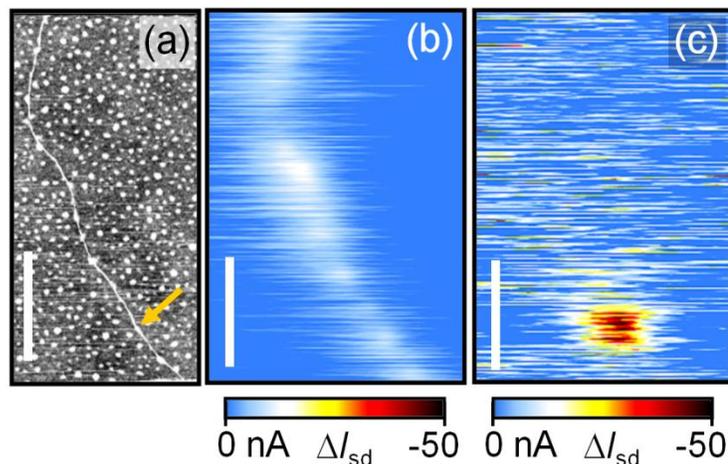
FIG. 3.3. (a) AFM topography. A defect was engineered in the CNT where indicated by the arrow. (b) Line-averaged scanning gate microscopy image before defect engineering and (c) after (V_{sd} = 50 mV, V_{bg} = -700 mV, V_{tip} = 3 V, *height* = 20 nm). Scale bars 1 μm.

Stable-defect device characteristics are shown in Fig. 3.4, 3.5, and 3.6. Each figure shows before-defect and after-defect low-bias transport characteristics representing the range of behavior that we have observed from quasi-metallic CNTs.

Figure 3.4 shows two devices for which the overall conductance decreased and n-type conductance was suppressed relative to p-type conductance (i.e. conductance at positive gate voltages was suppressed relative to the conductance at negative gate voltages). We also observed a notable increase in conductance fluctuations after

incorporation of the defect. Of the 15 defect devices we have characterized, 8 were qualitatively similar to Fig. 3.4.
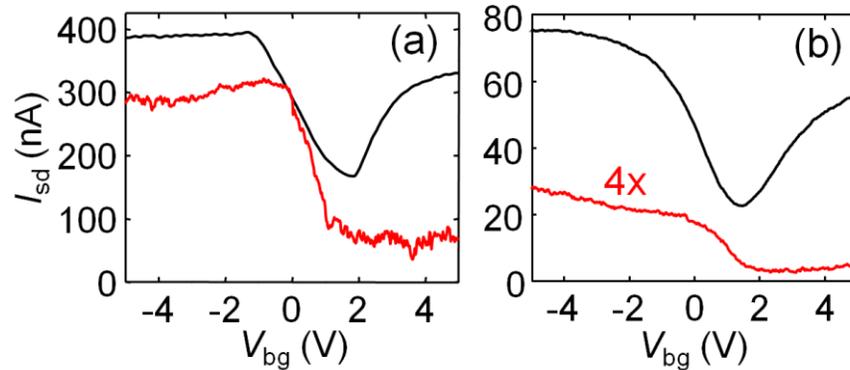
FIG. 3.4. Transistor response of two CNT FET devices before (black) and after (red) defect engineering. The red curves are the average of a few $I_{sd}(V_{bg})$ sweeps. In panel (b) the red curve is multiplied by four. ($V_{sd} = 25$ mV).

Figure 3.5 shows two devices where the point defect modification resulted in a minimal conductance change at most gate voltages, but caused sharp conductance dips at specific gate voltages. In addition, when V_{bg} was in the vicinity of one of these dips we sometimes observed random telegraph noise.[33] Five out of 15 devices were qualitatively similar to Fig. 3.5.
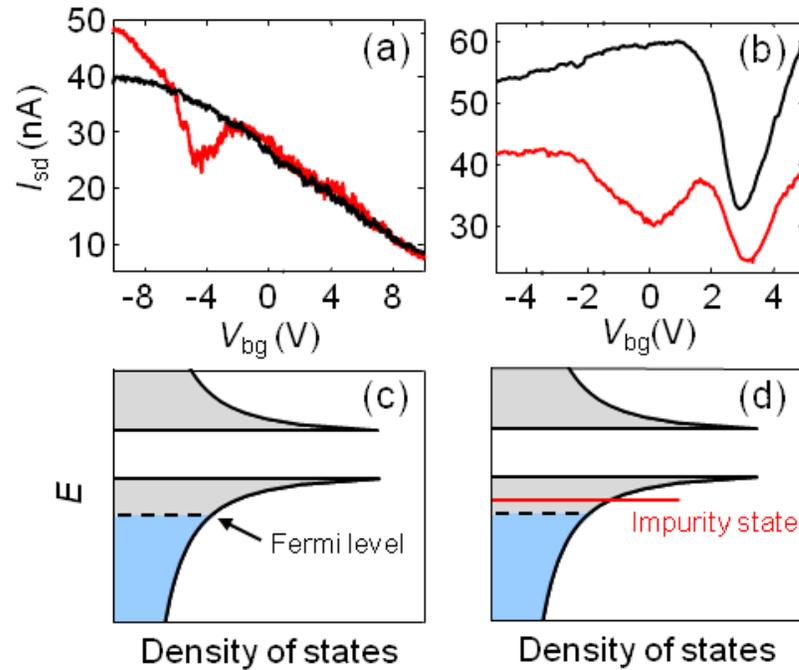
FIG. 3.5. Resonant scattering behavior. (a & b) Transistor characteristics of two CNT devices before (black) and after (red) defect engineering. ($V_{sd} = 25$ mV). The red curves are the average of a few $I_{sd}(V_{bg})$ sweeps. (c) Density of states of a pristine CNT. (d) Local density of states of a CNT around a neutral defect.

Lastly, Figure 3.6 shows a device where n-type conductance is heavily suppressed and a sharp peak emerges in the $I_{sd}(V_{bg})$ characteristics. Two out of 15 devices were qualitatively similar to Fig. 3.6. A third CNT device showed characteristics similar to the post-defect data in Fig. 3.6. However, no defect engineering was performed on the third device leading us to suspect a point defect occurred naturally.
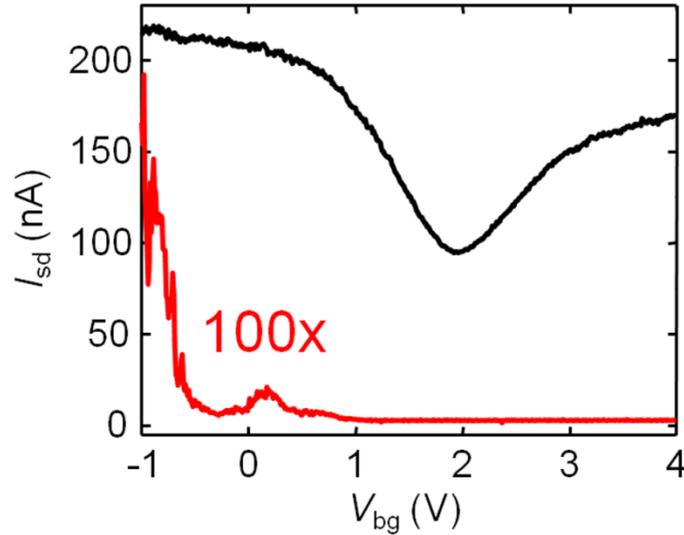
FIG. 3.6. Transistor characteristics of a CNT FET device before (black) and after (red) defect engineering. The red curve is multiplied by 100. (V_{sd} = 25 mV).

We first discuss the breaking of the symmetry between electron transport and hole transport that is seen in Figure 3.4. Suppression of n-type conductance has been observed previously,[1,20] and theoretical explanations have been sought.[7] Ashraf, et al. performed band structure calculations of CNTs containing clusters of covalently bound oxygen defects.[7] These calculations predict that certain cluster arrangements of multiple defects can suppress n-type conductance by a resonant scattering mechanism. However, this proposed mechanism does not explain the ubiquitous nature of suppressed n-type conductance that we observe.

We hypothesize that suppression of n-type conductance is related to the negative charge of oxidative point defects. Oxygen is more electronegative than carbon and, therefore, all oxidative defects carry some negative charge. The point defect structure with highest charge is likely a deprotonated carboxyl group (COO⁻), which is charged to $-e$ (the charge of an electron). The Coulomb potential from a negative charge will be a barrier to electron transport in small bandgap CNTs, but not to hole transport.

To test the importance of the defect charge, we model the electrostatic potential near the defect as a screened Coulomb potential. Figure 3.7a illustrates the specific case of a CNT with band gap of 180 meV and a charge $-e$ placed z = 1.5 nm from the long axis of the CNT such that the potential along the CNT axis is given by

$$V(x) = \frac{1}{4\pi\varepsilon_0} \frac{-e}{\sqrt{x^2 + z^2}} e^{-\sqrt{x^2 + z^2}/\lambda}$$

where λ is the electrostatic screening length set by the environment.

For the electrostatic potential shown in Fig 3.7a, we computed electron transmission probability at various energies, $T(E)$, using numerical Verlet integration of Schrödinger's equation. In this technique a plane wave solution is assumed for the transmitted wave and the remainder of the function is numerically constructed from the second derivative available from the Schrödinger equation. We use an electron effective mass of $m_e/50$, consistent with the 180 meV bandgap. Figure 3.7a shows a typical electron wave function tunneling through the barrier from left to right. The standing wave on the left side of the barrier is a result of interfering incident and reflected waves.
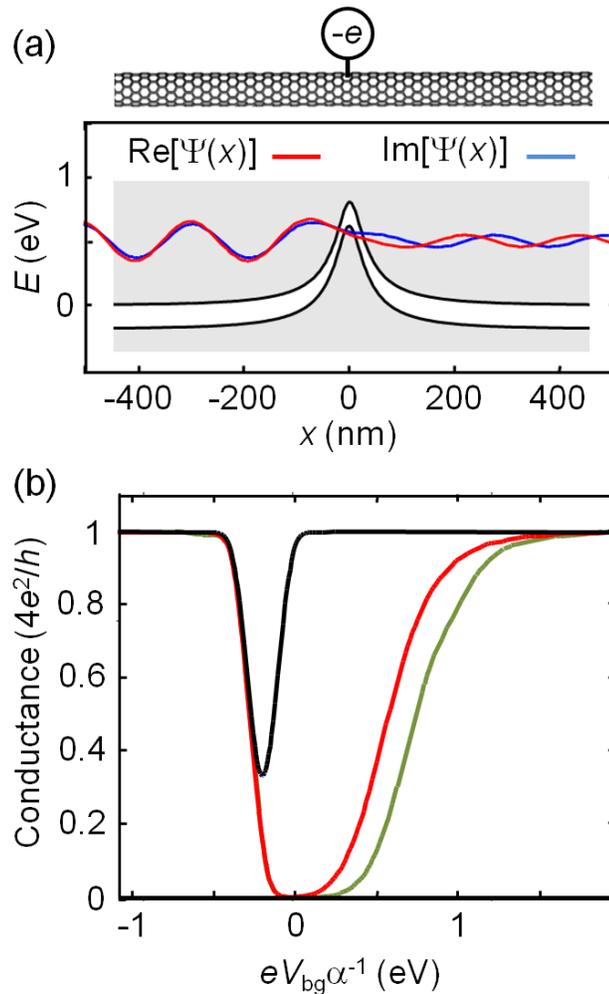
FIG. 3.7. Theoretical results. (a) A typical electron wave function, $\Psi(x)$, tunneling through a Coulomb barrier formed by a charged defect in a small band-gap CNT. The real and imaginary parts of the wave function are shown. (b) Conductance with and without a Coulomb barrier assuming perfect transmission through the rest of the device. The Fermi level in the CNT is set by $eV_{bg}\alpha^{-1}$, where α is the gate coupling constant. The black curve is calculated without a Coulomb barrier (no band bending), and the red and green curves correspond to Coulomb barriers with screening lengths of 8 nm and 1 μm, respectively. The calculation assumes electron effective mass = $m_e/50$, CNT band gap = 180 meV, $k_BT = 25$ meV, defect charge = $-e$, position of charge = 1.5 nm above the CNT axis.

Figure 3.7b shows the predicted conductance of the defect calculated from $T(E)$. Conductance as a function of gate voltage for a pair of 1D channels is calculated from the Landauer-Buttiker formalism

$$I = \frac{2}{e}\left(\frac{2e^2}{h}\right)\int_{-\infty}^{\infty} T(E)f(E,V_{bg}\alpha^{-1})[1-f(E-eV_{sd},V_{bg}\alpha^{-1})]dE$$

where $2e^2/h$ is the conductance quantum, $f(E,V_{bg}\alpha^{-1})$ is the Fermi-Dirac distribution function at room temperature, α is the gate coupling constant, and $eV_{bg}\alpha^{-1}$ sets the Fermi level in the CNT. Ambipolar behavior (symmetrical conductance for hole doping and electron doping) is predicted for the pristine CNT. Strongly suppressed conductance for electron doping is predicted when a negatively charged defect is present. These modeling results suggest that defect charge is indeed an important factor when considering electron transport through oxidative defects and can qualitatively explain the broken electron-hole symmetry seen in Fig. 3.4.

We next consider the sharp dips and peaks in the transport characteristics shown in Fig. 3.5 and 3.6, which we hypothesize are a result of the localized electronic states associated with a defect. Band structure calculations for CNTs with point defects predict the formation of localized impurity states.[7,8,9,10,11,12,13] These states have been experimentally observed in the local density of states around CNT defects, as measured with a scanning tunneling microscope.[27,34,35,36] Theoretical work has predicted that such impurity states will cause resonant scattering in electron transport measurements.[7,14] As the gate voltage modulates the Fermi level in a CNT, charge carriers may become resonant with impurity states as illustrated in Fig. 3.5c and 3.5d. Resonant scattering behavior is expected if the Fermi level aligns with an energy level that is within the conduction or valance band. Resonant scattering is a likely explanation for the sharp dips in conductance seen in Fig. 3.5. Alternatively, we expect resonant tunneling behavior (sharp peaks in the conductance) if there is a Coulomb barrier impeding electron transport and the Fermi level aligns with an impurity state in the bandgap (Fig. 3.8). Resonant tunneling is a possible explanation for the apparent peaks seen in Fig. 3.6.
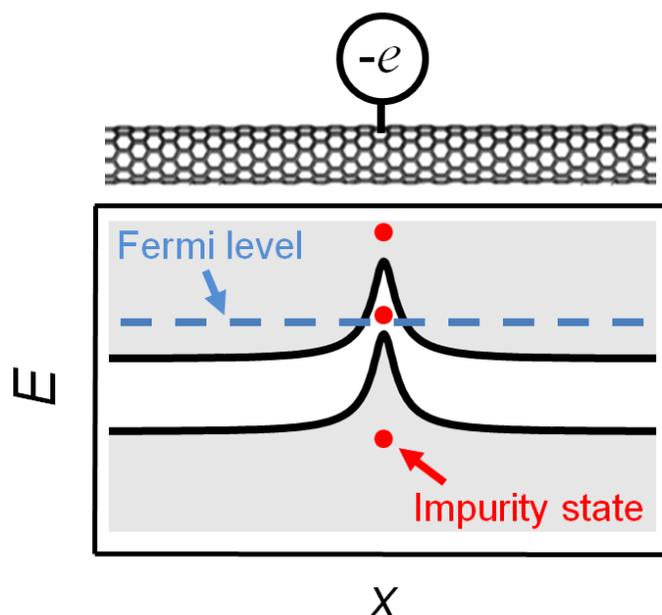
FIG. 3.8. Proposed resonant tunneling mechanism. The Fermi level aligns with an impurity state within the band gap of a Coulomb barrier.

The energy level structure of a CNT impurity state depends on the chiral index of the CNT and the chemical composition of the defect. Because of these unknowns, we cannot directly compare our experimental results to theory. However, we expect that further theoretical and experimental work will lead to the development of low-bias electron transport as a spectroscopic tool for identifying the chemical nature of oxidative point defects in CNTs. This would include experimental measurements of impurity state spectra for known defect types (to be determined independently). Theoretical modeling should also be applied to predict the impurity energy spectrum associated with different chemical defects.

3.5 Conclusion

We conclude that the AFM method of incorporating point defects in CNTs leads to a range of different defect types with distinct electrical characteristics. Our modeling of electron transport through a Coulomb barrier shows that the charge of the defect, which varies based on chemical structure, strongly influences electrical characteristics. Our measurements of resonant scattering and tunneling suggest that the spectrum of

impurity state energy levels associated with a defect also strongly influences electrical characteristics. Future work will aim for greater control over the defect generation process and more detailed theory to match the chemical structure of a defect with its electron transport signature.

3.6 Acknowledgements

References and Notes

1. Goldsmith, B.R. *et al.* Conductance-Controlled Point Functionalization of Single-Walled Carbon Nanotubes. *Science* **315**, 77-81 (2007).

2. Sorgenfrei, S. *et al.* Label-free single-molecule detection of DNA-hybridization kinetics with a carbon nanotube field-effect transistor. *Nat Nano* **6**, 126-132 (2011).

3. Robinson, J.A., Snow, E.S., Bădescu, Ş.C., Reinecke, T.L. & Perkins, F.K. Role of Defects in Single-Walled Carbon Nanotube Chemical Sensors. *Nano Letters* **6**, 1747-1751 (2006).

4. Buchs, G., Ruffieux, P., Gröning, P. & Gröning, O. Defect-induced negative differential resistance in single-walled carbon nanotubes. *Applied Physics Letters* **93**, 073115 (2008).

5. Tolvanen, A. *et al.* Modifying the electronic structure of semiconducting single-walled carbon nanotubes by Ar^+ ion irradiation. *Phys. Rev. B* **79**, 125430 (2009).

6. Buchs, G., Ruffieux, P., Gröning, P. & Gröning, O. Scanning tunneling microscopy investigations of hydrogen plasma-induced electron scattering centers on single-walled carbon nanotubes. *Applied Physics Letters* **90**, 013104 (2007).

7. Ashraf, M.K., Bruque, N.A., Pandey, R.R., Collins, P.G. & Lake, R.K. Effect of localized oxygen functionalization on the conductance of metallic carbon nanotubes. *Phys. Rev. B* **79**, (2009).

8. da Silva, L.B., Fagan, S.B. & Mota, R. Carboxylated Carbon Nanotubes under External Electrical Field: An Ab Initio Investigation. *The Journal of Physical Chemistry C* **113**, 8959-8963 (2009).

9. Carneiro, M.A., Venezuela, P. & Fagan, S.B. First Principles Calculations of Alanine Radicals Adsorbed on Pristine and Functionalized Carbon Nanotubes. *The Journal of Physical Chemistry C* **112**, 14812-14815 (2008).

10. Rocha, A.R., Padilha, J.E., Fazzio, A. & da Silva, A.J.R. Transport properties of single vacancies in nanotubes. *Phys. Rev. B* **77**, 153406 (2008).

11. Zhao, J., Park, H., Han, J. & Lu, J.P. Electronic Properties of Carbon Nanotubes with Covalent Sidewall Functionalization. *The Journal of Physical Chemistry B* **108**, 4227-4230 (2004).

12. Zhao, J. *et al.* Engineering the Electronic Structure of Single-Walled Carbon Nanotubes by Chemical Functionalization. *ChemPhysChem* **6**, 598-601 (2005).

13. Veloso, M.V., Souza Filho, A.G., Mendes Filho, J., Fagan, S.B. & Mota, R. Ab initio study of covalently functionalized carbon nanotubes. *Chemical Physics Letters* **430**, 71-74 (2006).

14. Choi, H.J., Ihm, J., Louie, S.G. & Cohen, M.L. Defects, Quasibound States, and Quantum Conductance in Metallic Carbon Nanotubes. *Phys. Rev. Lett.* **84**, 2917 (2000).

15. Hou, P.-X., Liu, C. & Cheng, H.-M. Purification of carbon nanotubes. *Carbon* **46**, 2003-2025 (2008).

16. Mawhinney, D.B. *et al.* Infrared Spectral Evidence for the Etching of Carbon Nanotubes: Ozone Oxidation at 298 K. *Journal of the American Chemical Society* **122**, 2383-2384 (2000).

17. Banerjee, S. & Wong, S.S. Rational Sidewall Functionalization and Purification of Single-Walled Carbon Nanotubes by Solution-Phase Ozonolysis. *The Journal of Physical Chemistry B* **106**, 12144-12151 (2002).

18. Coroneus, J.G. *et al.* Mechanism-Guided Improvements to the Single Molecule Oxidation of Carbon Nanotube Sidewalls. *ChemPhysChem* **9**, 1053-1056 (2008).

19. Kanai, Y., Khalap, V.R., Collins, P.G. & Grossman, J.C. Atomistic Oxidation Mechanism of a Carbon Nanotube in Nitric Acid. *Phys. Rev. Lett.* **104**, 066401 (2010).

20. Goldsmith, B.R., Coroneus, J.G., Kane, A.A., Weiss, G.A. & Collins, P.G. Monitoring Single-Molecule Reactivity on a Carbon Nanotube. *Nano Letters* **8**, 189-194 (2008).

21. Miyata, Y., Maniwa, Y. & Kataura, H. Selective Oxidation of Semiconducting Single-Wall Carbon Nanotubes by Hydrogen Peroxide. *The Journal of Physical Chemistry B* **110**, 25-29 (2006).

22. Peng, Y. & Liu, H. Effects of Oxidation by Hydrogen Peroxide on the Structures of Multiwalled Carbon Nanotubes. *Industrial & Engineering Chemistry Research* **45**, 6483-6488 (2006).

23. Kundu, S., Wang, Y., Xia, W. & Muhler, M. Thermal Stability and Reducibility of Oxygen-Containing Functional Groups on Multiwalled Carbon Nanotube Surfaces: A Quantitative High-Resolution XPS and TPD/TPR Study. *The Journal of Physical Chemistry C* **112**, 16869-16878 (2008).

24. Wepasnick, K.A., Smith, B.A., Bitter, J.L. & Howard Fairbrother, D. Chemical and structural characterization of carbon nanotube surfaces. *Anal Bioanal Chem* **396**, 1003-1014 (2010).

25. Park, J.-Y. Electrically tunable defects in metallic single-walled carbon nanotubes. *Appl. Phys. Lett.* **90**, 023112-3 (2007).

26. Park, J.-Y., Yaish, Y., Brink, M., Rosenblatt, S. & McEuen, P.L. Electrical cutting and nicking of carbon nanotubes using an atomic force microscope. *Appl. Phys. Lett.* **80**, 4446-4448 (2002).

27. Berthe, M. *et al.* Reversible Defect Engineering of Single-Walled Carbon Nanotubes Using Scanning Tunneling Microscopy. *Nano Letters* **7**, 3623-3627 (2007).

28. Kong, J., Soh, H.T., Cassell, A.M., Quate, C.F. & Dai, H. Synthesis of individual single-walled carbon nanotubes on patterned silicon wafers. *Nature* **395**, 878-881 (1998).

29. Leng, Y. Molecular charge mapping with electrostatic force microscope. *Proceedings of SPIE* 35-39 (1993).doi:10.1117/12.146383

30. Tans, S.J. & Dekker, C. Molecular transistors: Potential modulations along carbon nanotubes. *Nature* **404**, 834-835 (2000).

31. Kim, D.-H., Koo, J.-Y. & Kim, J.-J. Cutting of multiwalled carbon nanotubes by a negative voltage tip of an atomic force microscope: A possible mechanism. *Phys. Rev. B* **68**, 113406 (2003).

32. Prisbrey, L., DeBorde, T., Park, J.-Y. & Minot, E.D. Controlling the function of carbon nanotube devices with re-writable charge patterns. *Appl. Phys. Lett.* **99**, 053125 (2011).

33. Liu, F. *et al.* Giant random telegraph signals in the carbon nanotubes as a single defect probe. *Appl. Phys. Lett.* **86**, 163102 (2005).

34. Buchs, G. *et al.* Creation of paired electron states in the gap of semiconducting carbon nanotubes by correlated hydrogen adsorption. *New J. Phys.* **9**, 275-275 (2007).

35. Kim, H. *et al.* Local electronic density of states of a semiconducting carbon nanotube interface. *Phys. Rev. B* **71**, 235402 (2005).

36. Lee, S. *et al.* Paired Gap States in a Semiconducting Carbon Nanotube: Deep and Shallow Levels. *Phys. Rev. Lett.* **95**, 166402 (2005).

CHAPTER 4

Modeling the electrostatic signature of single enzyme activity

L. Prisbrey, G. Schneider, and E. D. Minot

Charge sensors based on nanoscale field-effect transistors are a promising new tool to probe the dynamics of individual enzymes. However, it is currently unknown whether the electrostatic signals associated with biological activity exceed detection limits. We report calculations of electrostatic signatures of two representative enzymes, deoxyribonuclease I and T4 lysozyme. Our simulations reveal that substrate binding to deoxyribonuclease and internal dynamics of lysozyme are detectable at the single-molecule level using existing point-functionalized carbon nanotube sensors.

4.1 Author's Note

The majority of the material contained in this chapter was published in 2010 in *The Journal of Physical Chemistry B* (**114**, 3330-3333 (2010) DOI: 10.1021/jp910946v). This chapter is a near duplication of that article, but also contains additional figures, data, and text for added clarity and a more thorough exploration of the topic. These additions do not appear as an independent supplemental section. Instead, they have been inserted into the main line text of the original article to preserve the readability of the chapter. To examine the journal approved text, or to cite this work, we refer the reader to original peer-reviewed publication.

4.2 Introduction

Enzyme function is closely linked to enzyme dynamics, and several techniques have been developed to probe this relationship. Nuclear magnetic resonance provides dynamic structural information but is an ensemble technique that cannot resolve the time sequence of events. Molecular dynamics simulations and single molecule fluorescence techniques[1] can elucidate the sequential nature of structural changes; however, the accessible time scales are limited. Molecular dynamics simulations running on supercomputers are still far from describing the whole turnover period of an enzyme (~1 ms), whereas single molecule fluorescence techniques are typically limited to time scales above 1 ms and less than a few seconds.

Nanoscale field effect transistors (nanoFETs) offer a new and complementary approach to track single-molecule activity by monitoring electrostatic fluctuations over a

wide range of time scales. Electronic detection of a single molecule reaction was recently demonstrated by continuous, multihour monitoring of a charge-sensitive, nanoscale field-effect transistor (nanoFET).[2] This achievement motivates our theoretical work exploring the use of nanoFET charge sensors as a new tool to study enzyme dynamics at the single-molecule level.

The conductance of a nanoFET device changes as a function of local electrostatic potential, allowing the proximity of charges to be monitored. In an early example of nanoFET biosensing, a carbon nanotube (CNT) FET was used to measure the activity of a small ensemble of glucose oxidase enzymes.[3] More recent CNT-based experiments have used point functionalization to localize the detection volume of the nanoFET.[4] Such a device was used to monitor a single carboxylate group interacting with its immediate environment.[2] It has been proposed that these point-functionalized devices are ideally suited for sensing the activity of a single enzyme tethered to the point defect.[2] The simulations presented below focus on this proposed geometry (Figure 4.1).
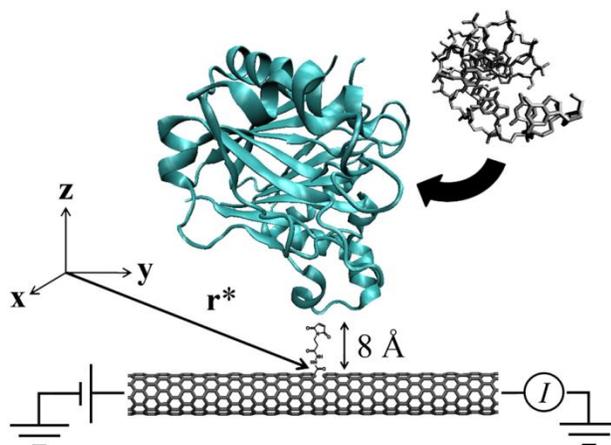
FIG. 4.1. DNase I (ribbon representation, colored blue) conjugated to an activated carboxyl group on a CNT using N-[β-maleimidopropionic acid]hydrazide (BMPH). The conjugation point on DNase I is a mutated residue 240 (G240C). The conductance of the device changes upon binding of the DNA fragment (stick representation). The figure is drawn to scale.

The magnitude of electrostatic fluctuations generated by a single enzyme is a critical unknown in nanoFET schemes for sensing enzyme dynamics. The point-functionalized CNT devices currently used in experiments require a change in local

electrostatic potential >10 mV to realize a conductance change that exceeds noise levels (within a 5 Hz−10 kHz bandwidth).[4] This 10 mV noise threshold can be obtained by comparing the magnitude of current noise from a nanoFET device with its transistor response. In this way, the corresponding gate voltage fluctuations can be found. Assuming that the defect acts a bottleneck for transport, the fluctuations in electrostatic potential at the defect are equal to these fluctuations in gate voltage. (We note that the 1/f dependence of the noise power spectral density in these sensors[4] allows for even faster sampling rates with little noise cost.) The electrostatics simulations presented in this work can be directly compared to this required minimum signal of 10 mV.

NanoFET sensors offer functionality similar to single molecule fluorescence; therefore, it is instructive to consider the limitations of a typical single-molecule fluorescence experiment. The enzyme β-galactosidase is a model system for the detection of individual turnover events. Using confocal microscopy, it is possible to monitor these individual events for tens of seconds. Single turnover resolution is lost when the turnover rate exceeds 370 s^{-1} and the maximum turnover rate of 740 s^{-1} is inaccessible.[5] Our work suggests that the nanoFET approach will allow many enzymes to be studied at turnover rates that are orders of magnitude faster than this single-molecule fluorescence example.

To determine the electrostatic signature of single-molecule activity, we have exploited computational methods developed for modeling electrostatics in biological systems.[6,7,8] We solve the nonlinear Poisson−Boltzmann equation (NPBE) for multiple enzyme conformations along an enzymatic pathway for two enzymes. The NPBE is given by

$$\nabla^2 \Phi = -\frac{4\pi}{\varepsilon}\rho - \frac{8\pi e[\text{salt}]}{\varepsilon}\sinh\left(\frac{e\Phi}{k_B T}\right)$$

where Φ is the electrostatic potential, ε is the dielectric constant, ρ is the charge density, e is the elementary charge, [salt] is the salt concentration, k_B is the Boltzmann constant, and T is the temperature. Three-dimensional maps of the electrostatic potential, $\Phi(\mathbf{r})$, around each enzyme structure was generated by solving this equation. The change in electrostatic potential, $\Delta\Phi$, associated with different enzymatic processes was found by comparing electrostatic potential maps for each structural configuration. This change in electrostatic

potential reflects the signal strength of the associated enzymatic process, which we compare to empirically derived device noise (discussed below). The first enzyme, deoxyribonuclease I (DNase I), is chosen to represent a class of enzymes in which the electrostatic signature of activity is expected to be dominated by the binding and unbinding of a charged substrate molecule. The second enzyme, T4 lysozyme (T4L), is chosen to represent a class of enzymes in which internal motion of charged protein regions is expected to dominate the electrostatic signature.

4.3 Methods

Figure 4.1 illustrates the geometry we have assumed for the nanoFET detection system. The enzyme is tethered site-specifically to the CNT defect using an 8-Å-long heterofunctional linker molecule (N-[β-maleimidopropionic acid]hydrazide) specifically designed to tether a cysteine residue to a carboxyl group. The coordinate **r*** denotes the position of the carboxyl defect. High-resolution crystal structures for DNase I[9] and T4L[10,11] were obtained from the Protein Data Bank, and charges were assigned to each atom of the enzyme using PDB2PQR[6,7] software employing the PARSE force field and using PROPKA to assign charges based on pKa values and pH. Extraneous atoms (solvent, extra copies of the molecules, etc.) were deleted from the unit cell to leave only the molecules of interest. Three-dimensional maps of the electrostatic potential $\Phi(\mathbf{r})$ were generated by solving the NPBE with a standard finite element technique using the Adaptive Poisson−Boltzmann Solver (APBS) software[8] on a desktop computer. All software is freely available. In all calculations, a single ion for each ion boundary condition was used for an initial $150 \times 150 \times 150$ Å box. This potential map was then used to set the Dirichlet boundary conditions for a smaller $75 \times 75 \times 75$ Å box. The grid points of this final map were spaced 0.4 Å apart. Ion radius was 2 Å. The relative dielectric constants were set to 78.5 for the water and 1.0 for the interior of the protein. Alternative values of the protein dielectric constant have been tested, as discussed below. The concentration of monovalent ions was varied from 1 to 150 mM to examine screening effects. Divalent ions were not considered in any of our calculations, since the

concentrations of Mg^{2+} and Ca^{2+} necessary for DNase and T4L activity (<100 μM) are well below the concentration of monovalent ions.

4.4 Results and discussion

We first examine the electrostatic signature expected from enzymatic activity of DNase I (Figure 4.1). The DNase I enzyme cleaves the backbone of double-stranded DNA. The DNA backbone is highly charged, so the substrate binding event is a promising candidate for charge-sensitive detection. For our calculations, we used a 2.0 Å crystal structure of wild type DNase I bound to a short DNA fragment (bare charge, $-12e$).[9] Charges were assigned to the enzyme at pH 7.5. Each phosphate group in the DNA fragment's backbone was assigned a charge of $-1e$, and the remaining atoms were left uncharged. It is well-known that counterion condensation reduces the bare charge of DNA.[12] The effect of counterion condensation is adequately described by the NPBE calculation of APBS.[13,14]

Our goal is to calculate changes in the electrostatic potential at the carboxyl defect, $\Delta\Phi(\mathbf{r}^*)$, when the DNA substrate binds to the enzyme. Two electrostatic potential volume maps were generated: the first describes the potential around the ligand-free enzyme, and the second describes the potential around the DNA−enzyme complex. The CNT and linker molecule were not included in the calculation (see discussion below). Residue 240 (GLY) was chosen as the site-specific immobilization point on the enzyme. It is an exposed residue near the active site and could conceivably be mutated into a cysteine without significantly altering the enzyme's structure (glycine and cysteine are similar in size, and both are nonpolar and uncharged). The coordinate $\mathbf{r}^*$ is set 8 Å from the α-carbon of residue 240 (8 Å is the length of the linker molecule) at a maximal distance from the protein surface. The distance between the bound DNA fragment and $\mathbf{r}^*$ is ~40 Å. At 1 mM monovalent ion concentration, we calculate $\Phi(\mathbf{r}^*) = -22$ mV for ligand-free DNase and $\Phi(\mathbf{r}^*) = -47$ mV for complexed DNase. The calculated change in potential associated with binding the negatively charged substrate $\Delta\Phi(\mathbf{r}^*)$ is therefore -25 mV.

The electrolyte concentration affects the ionic screening length and therefore affects $\Delta\Phi(\mathbf{r}^*)$. Following the procedures described above, we have calculated $\Delta\Phi(\mathbf{r}^*)$ over a range of salt concentrations. Figure 4.2 shows $\Delta\Phi(\mathbf{r}^*)$ (square data points) plotted as a function of Debye screening length,

$$\lambda_D = 9.62\text{\AA}\sqrt{\frac{100\,\text{mM}}{[\text{salt}]}}$$

The magnitude of $\Delta\Phi(\mathbf{r}^*)$ exceeds the 10 mV noise threshold when $\lambda_D > 33$ Å ([salt] < 8 mM). We note that DNase I is highly active in this range of monovalent ion concentrations.
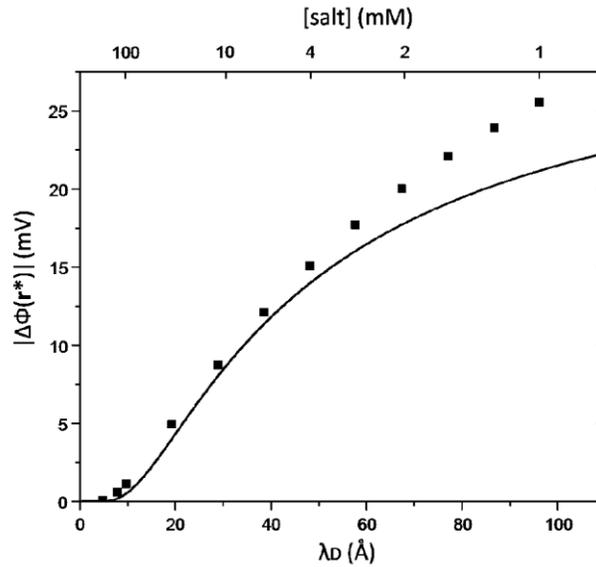
FIG. 4.2. The electrostatic signal, $\Delta\Phi(\mathbf{r}^*)$, when the DNA fragment binds to DNase I. The solid line shows the approximation $\Delta\Phi_{\text{Coulomb}}(\mathbf{r}^*)$ given by eq 4.1.

The calculated electrostatic signal at small λ_D is consistent with a screened Coloumb potential (Figure 4.2, solid line)

$$\Delta\Phi_{\text{Coulomb}}(\mathbf{r}^*) \cong \frac{1}{4\pi\varepsilon}\frac{q_{\text{DNA}}}{r}e^{-r/\lambda_D} \qquad (4.1)$$

where $r = 40$ Å and the DNA fragment's effective charge, q_{DNA}, is $-7e$. The effective charge was determined independently by accounting for counterion condensation on the DNA backbone. The solvent accessible surface area of each phosphate group was calculated. A buried group retains its bare charge of $-1e$, and a fully exposed group

experiences a 75% reduction in charge due to counterion condensation.[15] Partially buried groups were assumed to retain a portion of their bare charge according to a linear relationship with exposed surface area. The deviations from $\Delta\Phi_{Coulomb}(\mathbf{r}^*)$ seen at lower salt concentrations (see Figure 4.2) are expected as counterion condensation becomes less significant.

The good agreement between the NPBE simulation and the Coulomb potential (eq 4.1) suggests that our simulation results are insensitive to the dielectric constant of the protein. Indeed, we found that varying the relative dielectric constant of the protein between two extremes (1 to 20)[16] changed the calculated signal by only 13%.

We interpret $\Phi(\mathbf{r}^*)$ as representative of the average electrostatic potential felt at the carboxyl defect of the CNT sensor. This interpretation is based on the following assumptions: (i) The region of charge sensitivity around the point defect is small. This is consistent with scanning tunneling microscope spectroscopy studies that show the defect's electronic state does not extend more than 10 Å along the CNT axis.[17] (ii) The presence of the CNT and linker chain do not significantly perturb the potential at $\mathbf{r}^*$. This assumption is partially justified by the small volume occupied by the linker chain and the discrete nature of the CNT defect state. Theoretical investigations of the precise electronic structure and screening properties of the defect state are ongoing. (iii) Changes in $\Phi(\mathbf{r}^*)$ due to thermal motion of individual protein residues happen at very fast time scales (<<0.1 μs) and can be suppressed by time averaging. (iv) Translational and rotational motion of the entire enzyme due to center-of-mass thermal motion is fast (~0.1 μs),[18] and time averaging these fluctuations will lead to a measured potential $\Phi(\mathbf{r}^*)$ at the nanoFET sensor.
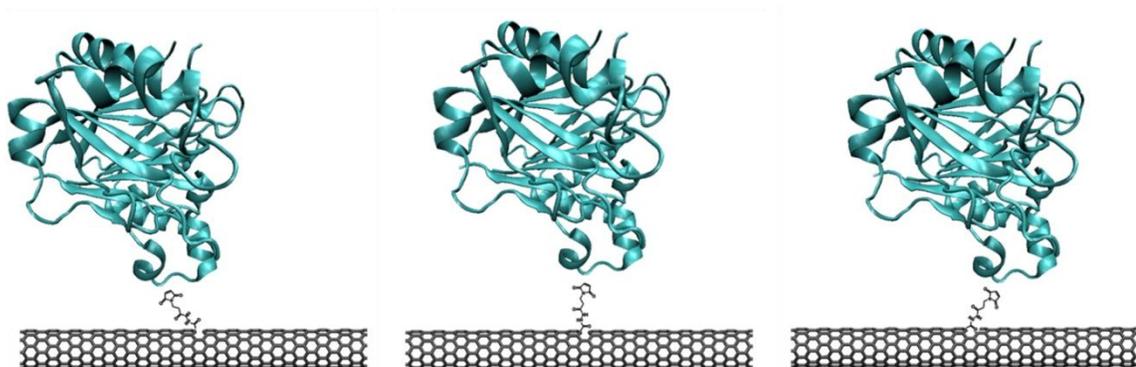
FIG. 4.3. Illustration of some possible positions that DNase I may sample while tethered to the carbon nanotube.

We have examined the final assumption in more detail to confirm that $\Phi(\mathbf{r}^*)$ is, indeed, representative of the potential after averaging over center-of-mass thermal motion. As the protein drifts the potential measured at the defect changes (Fig 4.3).
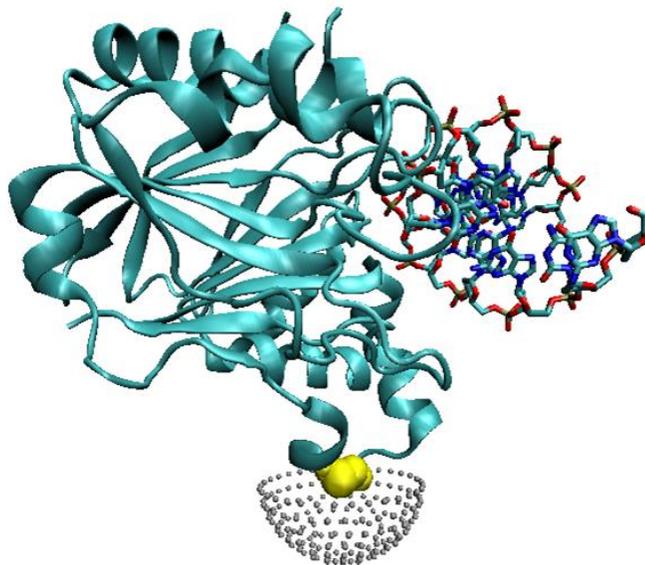
FIG. 4.4. DNase I (ribbon representation) bound to DNA (stick representation). The electrostatic potential, $\Phi(\mathbf{r})$, was calculated at each solvent accessible point 8 Å from residue 240. These points are indicated as gray spheres. Residue 240 atoms are represented with yellow spheres.

For ligand-free and DNA-bound DNase I in 1 mM ionic buffer, we calculated $\Phi(\mathbf{r})$ at 180 equally spaced solvent accessible points located 8 Å from residue 240 (the points

cover a solid angle of 1.8π) (Fig 4.4). The resulting distributions of potential are approximately Gaussian. Figure 4.5 shows the calculated distribution for ligand-free DNase I. The ligand-free form has a standard deviation of 17 mV and an average value of −21 mV, in close agreement with $\Phi(r^*)$ = −22 mV reported above. The DNA-bound form has a standard deviation of 18 mV and an average value of −50 mV, also in close agreement with the value reported above $\Phi(r^*)$ = −47 mV. The large standard deviations show that averaging over center-of-mass thermal motion time scales will be critical when looking for electrostatic signatures near the 10 mV minimum.
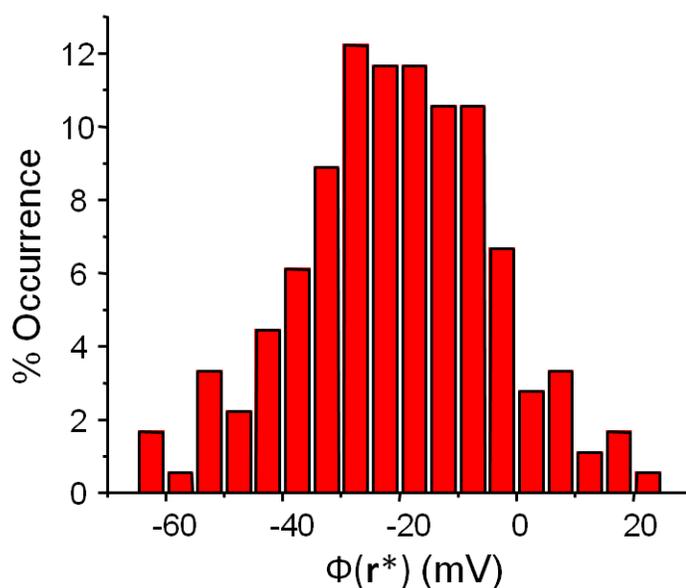
FIG. 4.5. The variation in electrostatic potential at the defect, $\Phi(r^*)$, as ligand-free DNase I samples various thermally accessible orientations. The the data shown here is calculated at the solvent accessible points indicated in figure 4.3.

We now turn to a second enzyme in which an electrostatic signature of biological activity may be generated by intrinsic dynamics rather than binding of a charged substrate. T4 lysozyme is an extensively studied enzyme known to exhibit a dramatic conformational change upon cleaving bacterial cell walls.[19,20] The T4L structure consists of two charged regions with net charges +3e and +7e. These regions move relative to each other in a hingelike motion (Figure 4.6). Single-molecule FRET studies suggest that this motion occurs on a millisecond time scale both with and without substrate present.[19]

T4L maintains high activity over a broad range of electrolyte concentrations ([salt] < 100 mM).[21] In our calculations, the closed state was represented by a 1.7 Å crystal structure of wild type T4L.[10] For the open state, a 2.0 Å crystal structure of the I3P mutant was used.[11] This mutant has been shown to be representative of the open state of wild type T4L along its enzymatic trajectory.[20] Residues 163 (ASN) and 164 (LEU) were removed from open T4L so that the two structures would contain exactly the same residues. Charges were assigned to each atom at pH 7.2. Because the I3P mutant has a different residue at position 3, residue 3 was neutralized in both structures.
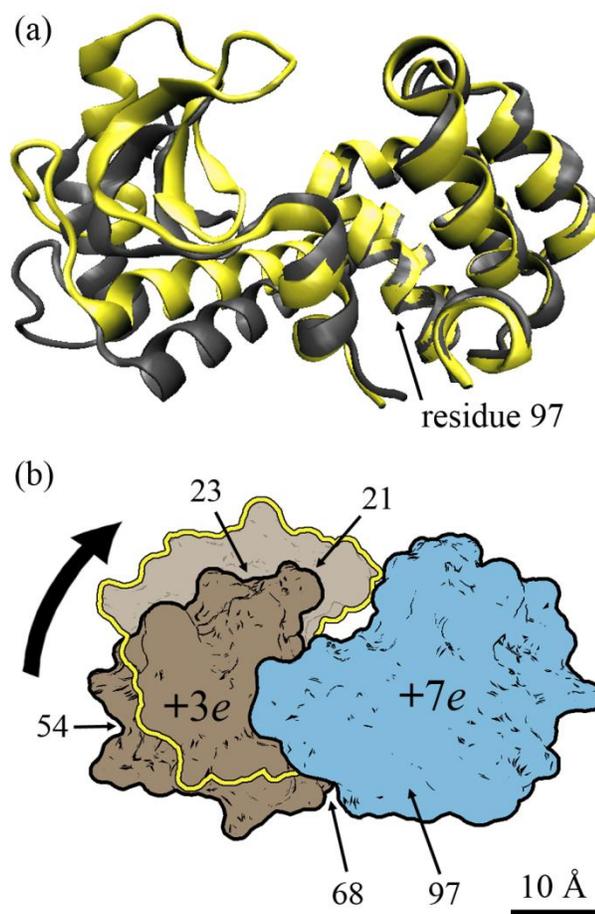
FIG. 4.6. (a) The open (gray) and closed (yellow) structures of T4 lysozyme used in our calculations (Protein Data Bank identification codes 4LZM and 1L97, respectively). The two structures were aligned using the protein backbone around residue 97 (α-carbons of residues 93−101). In this alignment, the +7e regions lie on top of each other, and the +3e region moves about the hinge point. (b) Cartoon illustrating the position of the +3e region relative to the +7e region of T4 lysozyme. In the open configuration, the +3e region is dark tan. In the closed-configuration the +3e region is outlined in yellow. Arrows point to

residues 21, 23, 54, 68, and 97, which were considered as possible site-specific attachment points.

A natural choice for a conjugation site in T4L is residue 97, an exposed cysteine with a 22 Å^2 molecular accessible surface area. Residue 97 is on the $+7e$ region of T4L; therefore, for our simulations, we align the $+7e$ regions of open and closed T4L (the near-perfect alignment is shown in Figure 4.3a). $\Phi(\mathbf{r})$ was calculated at $\mathbf{r}^*$, a point 8 Å away from the sulfur atom of residue 97, which maximized the distance between $\mathbf{r}^*$ and the protein surface. As a control experiment, we also calculated $\Phi(\mathbf{r}^*)$ when all charged residues in the $+7e$ region are neutralized. The results for 1 mM ionic buffer are show in Table 4.1.

TABLE 4.1.   The Electrostatic Potential at the CNT Defect Site $\Phi(\mathbf{r}^*)$ for Each T4L Structure with 1 mM Monovalent Ion Concentration

$\Phi(\mathbf{r}^*)$ (mV)	full calculation	control calculation (+7e region neutralized)
open	61	-13
closed	74	-1
difference	13	12

Figure 4.7 shows the effect of varying λ_D on $\Delta\Phi(\mathbf{r}^*)$. It can be seen that the calculated change in potential between open and closed T4L exceeds the 10 mV noise limit for $\lambda_D > 13$ Å ([salt] < 55 mM). The control calculation (Table 4.1) shows that this signal can be attributed to large-scale motion of the $+3e$ region, rather than small-scale redistribution of atoms within the $+7e$ region.
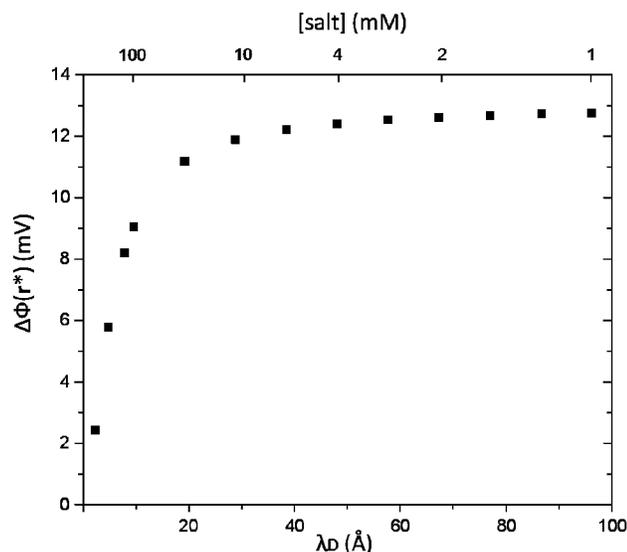
FIG. 4.7. Effect of salt concentration on $\Delta\Phi(\mathbf{r}^*)$ for the intrinsic motion of T4 lysozyme.

Modeling the T4L system with a simple Coulomb potential (eq 4.1) is inadequate for predicting $\Delta\Phi(\mathbf{r}^*)$. The signal from T4L activity originates from movement of a complicated spatial distribution of charge, in contrast to the DNase/DNA system in which the DNA fragment can be approximated as a localized charge. The charge distribution associated with T4L must be described in detail to make a reasonable estimate of $\Delta\Phi(\mathbf{r}^*)$. As was done with the DNase system, we calculated the fluctuations in $\Phi(\mathbf{r}^*)$ associated with center-of-mass thermal motion. For open and closed T4L in 1 mM ionic buffer, we calculated $\Phi(\mathbf{r})$ at approximately 60 equally spaced solvent-accessible points located 8 Å from residue 97 (these solvent-accessible points cover a solid angle of 0.7π). The resulting distributions are Gaussian-like and have means and standard deviations of 64 ± 11 mV for open T4L and 82 ± 15 mV for closed T4L. These average values agree with those reported in Table 1. The large standard deviations reinforce our conclusion that single-molecule sensing in the proposed nanoFET geometry will be limited to time scales slower than center-of-mass thermal motion time scales.

Even without optimizing the residue choice for site-specific immobilization, our calculations show that the hinge motion dynamics of T4L is potentially detectable with a nanoFET sensor. In an attempt to optimize signal strength, simulations were preformed for four different conjugation sites on the $+3e$ region. At a monovalent ion concentration

of 1 mM, the calculated signal strengths were 10 mV (residue 21), 11 mV (residue 23), 0.4 mV (residue 54), and 5 mV (residue 68). Conveniently, the naturally occurring exposed cysteine (residue 97) gives the largest signal.

4.5 Conclusion

Our calculations show that the processes of substrate binding to DNase I and internal dynamics of T4L could be detected with a point-functionalized CNT sensor. At physiological salt concentrations ([salt] ~ 100 mM), signals are below the limits of detection for existing devices; therefore, we conclude that the general applicability of these sensors is currently limited to (i) studying enzymes that are active when salt concentrations are lower than physiological conditions (DNase I and T4L are both active at appropriately low salt concentrations) and (ii) studying enzyme processes involving highly charged substrate molecules. Although our modeling shows that the time resolution of single-molecule nanoFET sensing will not exceed the time scales of center-of-mass thermal motion, the predicted time resolution (~1 μs) is significantly faster than existing single-molecule techniques. We expect that application of our computational methods to more enzyme systems will reveal many biologically relevant single-molecule processes that are potentially detectable with nanoFET detection schemes. Additional applications of these computational methods will include the prediction of signals from nanoFET-based immunoassay sensors.[22]

4.6 Acknowledgments

References and Notes

1. Blank, K., Gert De Cremer & Johan Hofkens Fluorescence-based analysis of enzymes at the single-molecule level. *Biotechnology Journal* **4**, 465-479 (2009).

2. Goldsmith, B.R., Coroneus, J.G., Kane, A.A., Weiss, G.A. & Collins, P.G. Monitoring Single-Molecule Reactivity on a Carbon Nanotube. *Nano Letters* **8**, 189-194 (2008).

3. Besteman, K., Lee, J.-O., Wiertz, F.G.M., Heering, H.A. & Dekker, C. Enzyme-Coated Carbon Nanotubes as Single-Molecule Biosensors. *Nano Letters* **3**, 727-730 (2003).

4. Goldsmith, B.R. et al. Conductance-Controlled Point Functionalization of Single-Walled Carbon Nanotubes. *Science* **315**, 77-81 (2007).

5. English, B.P. et al. Ever-fluctuating single enzyme molecules: Michaelis-Menten equation revisited. *Nat Chem Biol* **2**, 87-94 (2006).

6. Dolinsky, T.J. et al. PDB2PQR: expanding and upgrading automated preparation of biomolecular structures for molecular simulations. *Nucleic Acids Research* **35**, W522-W525 (2007).

7. Dolinsky, T.J., Nielsen, J.E., McCammon, J.A. & Baker, N.A. PDB2PQR: an automated pipeline for the setup of Poisson-Boltzmann electrostatics calculations. *Nucleic Acids Research* **32**, W665-W667 (2004).

8. Baker, N.A., Sept, D., Joseph, S., Holst, M.J. & McCammon, J.A. Electrostatics of nanosystems: Application to microtubules and the ribosome. *Proceedings of the National Academy of Sciences* **98**, 10037 -10041 (2001).

9. Lahm, A. & Suck, D. DNase I-induced DNA conformation : 2 Å Structure of a DNase I-octamer complex. *Journal of Molecular Biology* **222**, 645-667 (1991).

10. Bell, J.A. et al. Comparison of the crystal structure of bacteriophage T4 lysozyme at low, medium, and high ionic strengths. *Proteins: Structure, Function, and Bioinformatics* **10**, 10-21 (1991).

11. Dixon, M.M., Nicholson, H., Shewchuk, L., Baase, W.A. & Matthews, B.W. Structure of a hinge-bending bacteriophage T4 lysozyme mutant, Ile3 --> Pro. *Journal of Molecular Biology* **227**, 917-933 (1992).

12. Manning, G.S. The Molecular Theory of Polyelectrolyte Solutions with Applications to the Electrostatic Properties of Polynucleotides. *Quarterly Reviews of Biophysics* **11**, 179-246 (1978).

13. Das, R. et al. Counterion Distribution around DNA Probed by Solution X-Ray Scattering. *Phys. Rev. Lett.* **90**, 188103 (2003).

14. Ballauff, M. & Jusufi, A. Anomalous small-angle X-ray scattering: analyzing correlations and fluctuations in polyelectrolytes. *Colloid Polym Sci* **284**, 1303-1311 (2006).

15. Keyser, U.F. et al. Direct force measurements on DNA in a solid-state nanopore. *Nat Phys* **2**, 473-477 (2006).

16. Warshel, A., Sharma, P.K., Kato, M. & Parson, W.W. Modeling electrostatic effects in proteins. *Biochimica et Biophysica Acta (BBA) - Proteins & Proteomics* **1764**, 1647-1676 (2006).

17. Berthe, M. et al. Reversible Defect Engineering of Single-Walled Carbon Nanotubes Using Scanning Tunneling Microscopy. *Nano Letters* **7**, 3623-3627 (2007).

18. We estimate the correlation time τ for the center-of-mass thermal motion of a tethered protein as the time the protein takes to diffuse a distance $x \approx 3$ nm ($\pi \times$ tether length). The diffusion time is given by $\tau = x^2/D$ where D is the diffusion constant of a small protein in water ($D \approx 10^{-6}$ cm^2/s).

19. Chen, Y., Hu, D., Vorpagel, E.R. & Lu, H.P. Probing Single-Molecule T4 Lysozyme Conformational Dynamics by Intramolecular Fluorescence Energy Transfer. *The Journal of Physical Chemistry B* **107**, 7947-7956 (2003).

20. Zhang, X.-jun, Wozniak, J.A. & Matthews, B.W. Protein Flexibility and Adaptability Seen in 25 Crystal Forms of T4 Lysozyme. *Journal of Molecular Biology* **250**, 527-552 (1995).

21. Priyadarshini, S. & Kansal, V.K. Biochemical Characterization of Buffalo (Bubalus Bubalis) Milk Lysozyme. *Journal of Dairy Research* **70**, 467-471 (2003).

22. Allen, B.L., Kichambare, P.D. & Star, A. Carbon Nanotube Field-Effect-Transistor-Based Biosensors. *Advanced Materials* **19**, 1439-1451 (2007).

CHAPTER 5

Controlling the function of carbon nanotubes with re-writable charge patterns

L. Prisbrey, T. DeBorde, J-Y. Park, and E. D. Minot

We use atomic force microscopy lithography to write charge patterns in close proximity to carbon nanotube field-effect transistor devices. The silicon dioxide substrate retains the charge for days, allowing various charge configurations to be tested. We show that the written charge can move the Fermi level in the nanotube by 1 eV and we use this charge lithography to reconfigure a field-effect transistor into a pn junction. The substrate charge can be erased and rewritten, offering a new tool for prototyping nanodevices and optimizing electrostatic doping profiles.

5.1 Author's Note

The majority of the material contained in this chapter was published in 2011 in *Applied Physics Letters* (**99**, 053125 (2011) DOI: 10.1063/1.3622138). This chapter is a near duplication of that article, but also contains additional figures, data, and text for added clarity and a more thorough exploration of the topic. These additions do not appear as an independent supplemental section. Instead, they have been inserted into the main line text of the original article to preserve the readability of the chapter. To examine the journal approved text, or to cite this work, we refer the reader to original peer-reviewed publication.

5.2 Introduction

The performance of nanoelectronic devices is highly dependent on charges in the surrounding environment. Surface charge traps give rise to device noise[2] and hysteresis,[3,4] while spatial variations in surface charge lead to gate-sensitive "hotspots" in nanoscale electronic devices[5] and light-sensitive "hotspots" in nanoscale optoelectronic devices.[6]

Previous authors have demonstrated that scanning probe lithography can be used to create charge patterns on a range of surfaces.[7,8,9,10] Such charge patterns have been used in nanoelectronics research, for example, to electrostatically define channels in a two-dimensional electron gas[7] or to create small electrostatic perturbations in carbon nanotube based field-effect transistor (CNT FET) devices.[11] In the work of Brunel et al.,[11] a conducting atomic force microscopy (AFM) tip was used to write a spot of charge on

the SiO_2 surface near a CNT FET. The charge-sensitive CNT device detected this small electrostatic perturbation and functioned as a non-volatile memory element.

Here, we show that charge patterns written on a SiO_2 surface can be used to controllably modulate the doping profile of a nanoelectronic device. We demonstrate electrostatic doping that corresponds to ± 1 eV shifts in the Fermi level of a CNT. To illustrate the power of this charge patterning technique, we define regions of positive and negative charges in close proximity to a CNT FET and create a pn junction device.

5.3 Methods

Individual CNT devices were made by patterning catalyst on a SiO_2/Si substrate (thermal oxide with thickness $t = 300$ nm) and growing CNTs by catalyzed chemical vapor deposition using a semi-automated growth system (Kevek Innovations).[12] Electrodes (Ti/Pt) were patterned by photolithography to produce circuits with ~10 nanotubes connected in parallel. Scanning probe experiments were performed in an AFM with a custom-built stage for in-situ electrical probing (Asylum Research MFP-3D). Electric force microscopy (EFM)[13] and scanning gate microscopy (SGM)[5] were used to identify a single desired CNT. The undesired CNTs were electrically cut with a Pt-coated AFM probe[14] resulting in a single CNT FET. A schematic of the geometry is shown in Fig. 5.1.
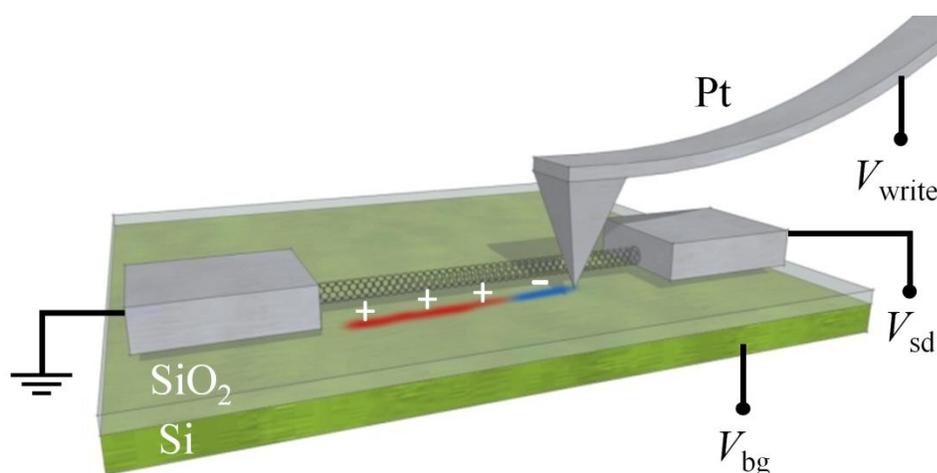
FIG. 5.1. Device schematic illustrating charge lithography near a CNT connected to two electrodes (not to scale). Charge is written ~300 nm from the CNT.

Charge patterns were written directly on the SiO_2 layer around the CNT FET with a biased, Pt-coated AFM probe, as illustrated in Fig. 5.1. We found that positive and negative tip bias, V_{write}, modified the surface charge when the probe was dragged across the surface (contact force ~6–9 nN). Figure 5.2 shows electric force microscopy images of a bare SiO_2 surface following writing and erasure. We used a variety of scanning probe techniques to investigate this surface charge and the effect it has on the nearby CNT FET.
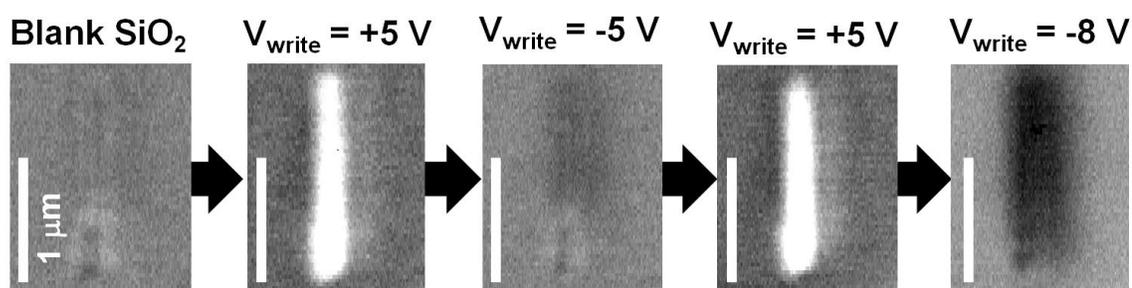
FIG. 5.2. Electric force microscopy images of a silicon oxide surface during various stages of charge lithography ($V_{tip} = 0$ V, *height* = 20 nm). The panels are arranged in chronological order. From left to right: a bare silicon oxide surface, following charge lithography with $V_{write} = +5$ V, erasure of previous charge with $V_{write} = -5$ V, redrawing of positive charge following erasure ($V_{write} = +5$V), and finally overwriting positive charge with negative charge ($V_{write} = -8$ V).

5.4 Results and discussion

Fig. 5.3a shows an electrically contacted CNT on a SiO$_2$ substrate. Arrows on the image show the path that was traced by the electrically biased AFM tip. A tip bias V_{write} = −10 V was used for the upper half of the CNT, and V_{write} = +10 V was used in the lower half. The back gate, source, and drain electrodes were grounded during charge writing. The regions where charge was written show up clearly in Kelvin force microscopy[15] (KFM) measurements, as shown in Fig. 5.3b. The KFM image confirms that negative charge was written at −10 V (the surface potential is more negative than the surrounding oxide) and positive charge was written at +10 V (the surface potential is more positive than the surrounding oxide).
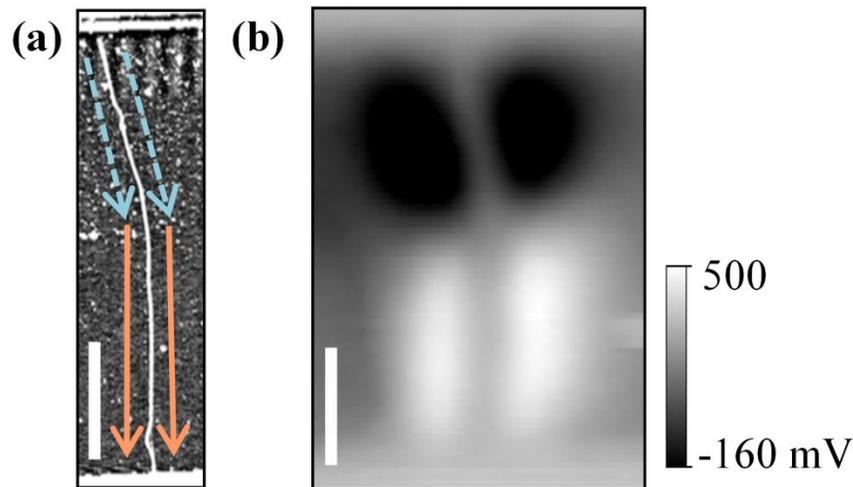
FIG. 5.3. Defining the charge pattern for a pn junction. (a) AFM topography of the CNT device with arrows indicating the lithography paths (dashed line indicates V_{write} = −10 V, solid line indicates V_{write} = +10 V). (b) Kelvin force microscopy image taken after the charge lithography (V_{bg} = 0 V, *height* = 25 nm). Scale bars are 1 μm.

The deposited surface charge has a dramatic effect on the doping profile of the nearby CNT. Fig. 5.4 shows SGM measurements taken before and after charge lithography. The SGM images are obtained by hovering the electrically biased AFM tip (the scanning gate) above the device and recording conductance as a function of tip position.[5] The image obtained before charge lithography shows a spatially uniform response to the scanning gate, with conductance increasing when the tip is close to the

CNT. After charge lithography, the SGM image shows that the upper and lower portions of the CNT respond differently to the scanning gate. Transistor curves taken before and after writing the charge also show a clear change (Fig. 5.4c). Initially, the device displayed typical small bandgap behavior with a single conductance minima at $V_{bg} = 4.3$ V. After charge lithography, the transistor curve has a double dip, with conductance minima on either side of $V_{bg} = 4.3$ V. Repeatedly sweeping Vbg from −1 to +10 V caused the two dips to approach each other and reform the original transistor curve.
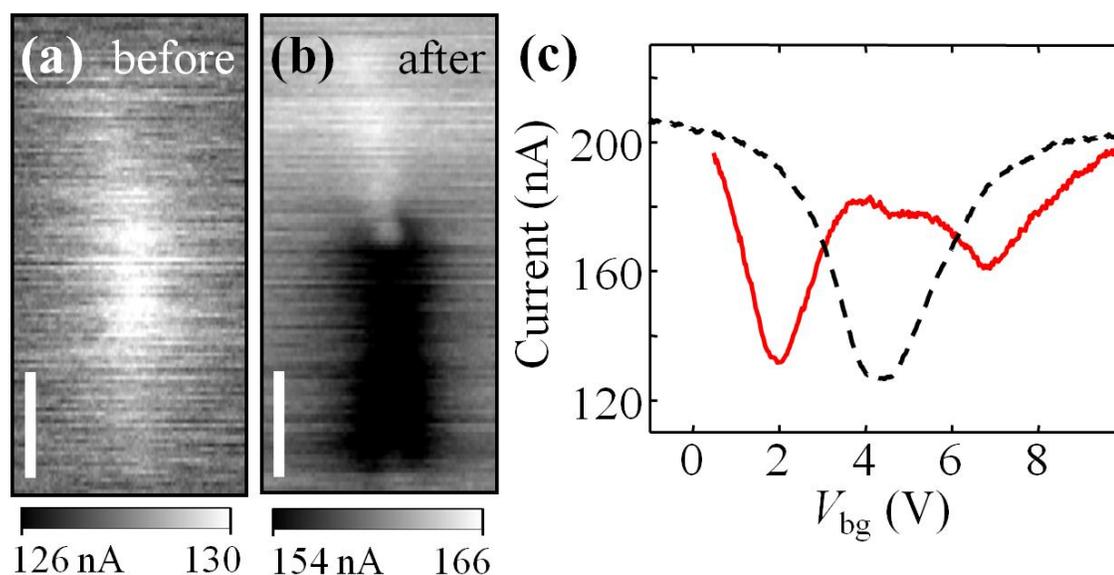
FIG. 5.4. Device characteristics following pn junction engineering. (a) Scanning gate microscopy image before charge writing ($V_{bg} = 2$ V, $V_{tip} = 0$ V, $V_{sd} = 25$ mV, *height* = 25 nm). (b) Scanning gate microscopy image after charge writing ($V_{bg} = 2.5$ V, $V_{tip} = -2$ V, $V_{sd} = 25$ mV, *height* = 25 nm). Scale bars are 1 µm in both images. (c) $I(V_{bg})$ of the device shown in (a) measured with $V_{sd} = 25$ mV. The dashed black line was measured before charge writing, the solid red line was measured after charge writing.

The SGM measurements indicate that doping along the length of the CNT is modified by the lithographically defined surface charge. The upper portion of the CNT becomes more conductive when the negatively biased tip approaches, indicating that the upper portion of the CNT is p doped. The lower portion of the CNT becomes less conductive when the negatively biased tip approaches, indicating that the lower portion of the CNT is n doped. The transistor curves (Fig. 5.4c) further verifies that the device

consists of p-type and n-type sections in series when $V_{bg} = 4.3$ V. Similar double-dip transistor curves have been observed from CNT devices that had spatially modulated doping profiles created by different means.[16]

Further measurements were carried out to confirm the presence of a pn junction device. Figure 5.5 shows $I(V_{sd})$ characteristics of a large bandgap CNT device following pn junction engineering (as illustrated in figure 5.3a). Before charge writing, the device exhibits typical large bandgap semiconductor behavior. Following pn junction engineering the device shows different characteristics.
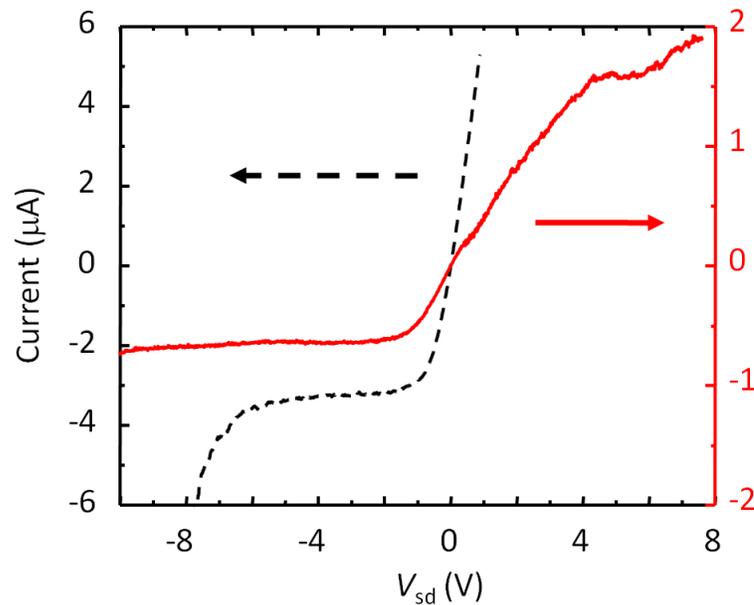
FIG. 5.5. Comparison of $I(V_{sd})$ characteristics before and after pn junction engineering. The dashed black line was measured before charge writing, the solid red line was measured after writing.

A signature of a pn junction is rectifying characteristics in the $I(V_{sd})$ curve. The curve taken following pn junction engineering (Fig 5.5, red) clearly shows rectifying behavior, indicating a pn junction was incorporated into the device. The curve is not well fit by the ideal Schockley diode equation. This is because the pn junction is connected in series with the n-doped and p-dope portions of CNT, both of which exhibit non-linear $I(V_{sd})$ response. At negative V_{sd} the resistance of the pn junction dominates the circuit resistance, and diode-like behavior is displayed. At positive V_{sd} the resistance of the pn

junction becomes very small compared to n-doped region of the CNT, and this behavior dominates. As stated above, as V_{sd} becomes very large doping is deteriorated, which is a likely explanation of the non-exponential rise at $V_{sd} \gg 100$ mV.

We also performed photocurrent measurements to verify the existence of the pn junction. In scanning photocurrent microscopy a laser spot is raster scanned along the surface and current through the circuit is recorded. Figure 5.6 shows short circuit scanning photocurrent microscopy data for a CNT device before and after pn junction engineering. Before charge lithography the device exhibits a response at the CNT-electrode interface (Fig 5.6b), and afterward another feature appears (Fig 5.6c).
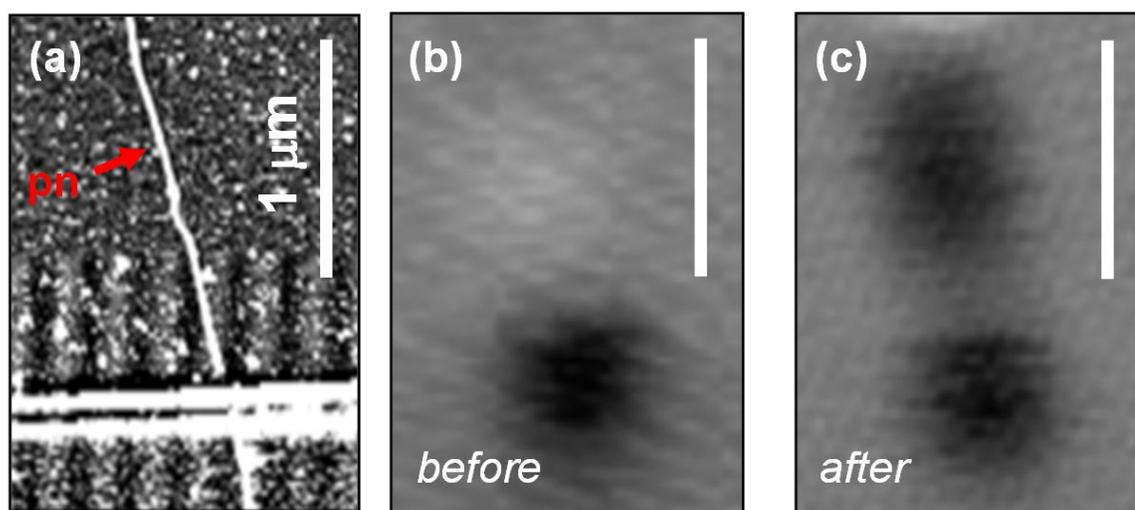
FIG. 5.6. Comparison of scanning photocurrent microscopy images taken before and after pn junction engineering. (a) AFM topography image. A pn junction was engineered at the location indicated by the arrow. (b) Scanning photocurrent microscopy image taken before and (c) after a pn junction was engineered in the device ($V_{sd} = 0$ V, HeNe *spot size* = 1 μm).

The scanning photocurrent response before lithography contains a feature at the connection between the CNT and the electrode. This affect is well known and is the result of the work function mismatch between the CNT and the electrode. At the CNT-electrode interface the energy bands must bend such that the Fermi level remains constant across the junction. The bent bands resemble a pn junction structure, and are known as a Shottkey diode. When the laser illuminates the junction electrons and holes are thermally

excited, and the 'built in' electric field of the pn junction separates them. These charges move through the unbiased circuit and are recorded. We interpret the new feature that appears following pn junction engineering (Fig 5.6c) as another diode with the same qualitative explanation as the Shottkey diode. This second diode-like response is the result of the pn junction engineered in the device through charge lithography.

Above we demonstrated the utility of the charge writing technique to engineer new nanoelectronic devices. We now turn our attention to quantifying these effects in more detail. To quantify the electrostatic doping seen in Fig. 5.4, we created a uniform doping profile along a CNT FET. The procedure was the same as outlined in Fig. 5.3a, except that $V_{write} = +10$ V was used throughout the process. Transistor curves measured before and after showed a maximum shift $\Delta V_{bg} = -5$ V (Fig. 5.7a). Subsequent sweeps of V_{bg} (numbered 1 to 12 in Fig. 5.4) caused the doping effect to decay.
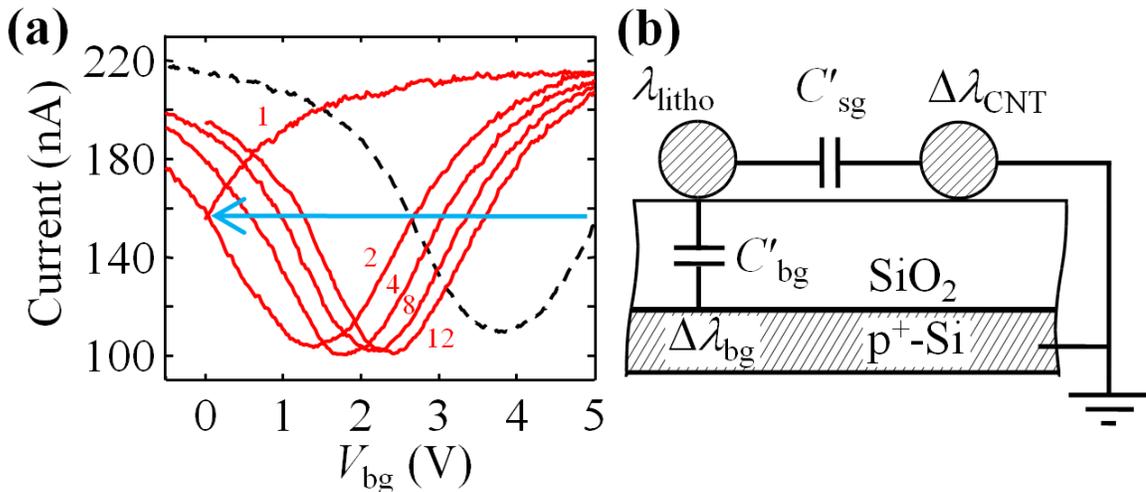
FIG. 5.7. Electrical characteristics before and after writing a uniform charge pattern. (a) The dashed black line shows $I(V_{bg})$ measured at $V_{sd} = 25$ mV before writing charge. The solid red lines show $I(V_{bg})$ at various times after writing charge ($V_{write} = +10$ V). The numbers refer to the number of V_{bg} cycles, for example, curve 4 was obtained on the 4th cycle of sweeping V_{bg}. (b) Equivalent circuit diagram illustrating the capacitive coupling between the lithographic charge, the CNT, and the silicon back gate.

From the observed shift, ΔV_{bg}, one can estimate the change in Fermi level in the CNT, ΔE_F, and the linear charge density, λ_{litho}, stored on the SiO_2 surface. First, we note

that the patterned charge is acting as a "side gate" and is equivalent to applying +5 V to the back gate. The charge per unit length that is induced in the CNT is then $\Delta\lambda_{CNT} = C'_{bg} \Delta V_{bg}$, where C'_{bg} is the back gate capacitance per unit length,[17]

$$C'_{bg} = \frac{2\pi\varepsilon\varepsilon_0}{\cosh^{-1}(t/r)} = 40\frac{aF}{\mu m}. \qquad (5.1)$$

For our device, the radius of the CNT is $r = 1.9$ nm, the relative dielectric constant of the SiO$_2$ is $\varepsilon = 4$, and the thickness of the dielectric $t = 300$ nm. We find $\Delta\lambda_{CNT} = 1200e$ μm^{-1}. This doping level can be expressed as a shift in the Fermi level of the CNT, $\Delta E_F = \Delta\lambda_{CNT}/eD$, where $D \approx 4/h\nu_F$ is the density of states of a single-walled CNT at energies above and below the bandgap (e is the charge of the electron, h is Plank's constant, and $\underline{\nu}_F = 8 \times 10^5$ m/s is the Fermi velocity). For our experiment, we find $\Delta E_F \sim 1$ eV. If larger doping levels were required, one could pattern additional lines of charge or decrease the separation distance between λ_{litho} and the CNT. However, $\Delta E_F = \pm 1$ eV is sufficient for most semiconductor devices that utilize doping modulation.

The magnitude of the patterned charge, λ_{litho}, is proportional to $\Delta\lambda_{CNT}$. The proportionality constant depends on the ratio of capacitances C'_{tot}/C'_{sg}, where C'_{tot} is the total capacitance between the patterned charge and nearby conducting objects and C'_{sg} is the "side gate" capacitance between the patterned charge and the CNT (Fig. 5.7b),

$$\lambda_{litho} = -\frac{\Delta\lambda_{CNT}}{2}\left(\frac{C'_{tot}}{C'_{sg}}\right).$$

The factor of 2 arises because two lines of charge were drawn, one on either side of the CNT. We estimate $C'_{sg} \sim 14$ aF/μm from the geometric capacitance between two parallel wires of radius $r \sim 1.9$ nm, separated by 300 nm and an effective dielectric environment $\varepsilon = 2.5$. Additional contributions to C'_{tot} are dominated by the capacitance between the patterned charge and the back gate which we estimate using Eq. (5.1). We conclude that $\lambda_{litho} \sim 2400e$ μm^{-1} when $V_{write} = +10$ V.

For practical applications of charge lithography, the lifetime of the charge pattern is an important consideration. We noted above that sweeping V_{bg} erases doping effects (Fig. 5.7a). If V_{bg} and V_{sd} are kept small ($\sim$100 mV), however, the doping effect persists for many days. Fig. 5.8a shows a long time trace from a CNT FET before and after

writing charge. Baseline conductivity was established during the first 6 hours. Charge was then written using $V_{write} = +10$ V so that the lithographic side gates uniformly doped the length of the CNT. Over the next 70 hours, the conductance tended toward its original value but never fully recovered. EFM measurements taken at $t = 70$ hours showed no sign of the written charge, and the lingering ΔV_{bg} was erased by sweeping V_{bg}.
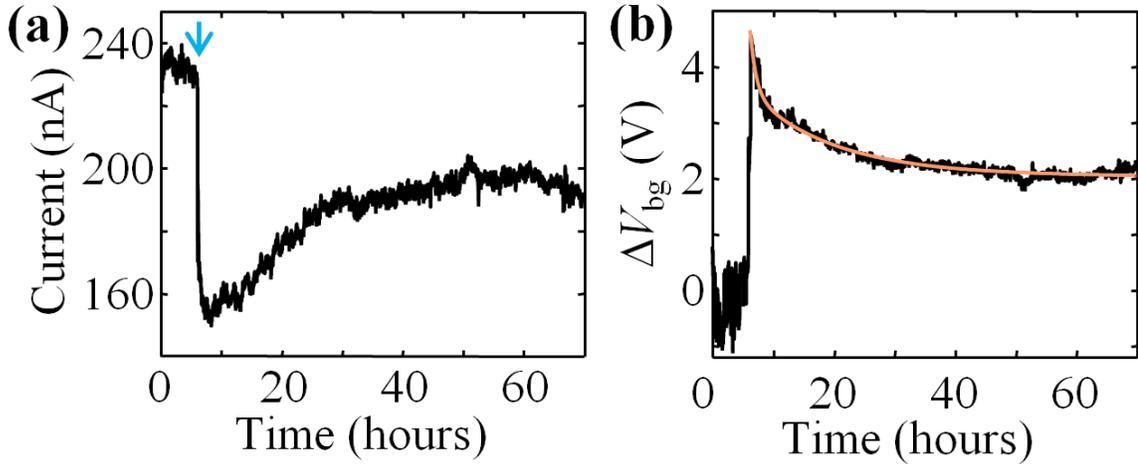
FIG. 5.8. Lifetime of the doping effect. (a) Current measured as a function of time at $V_{bg} = 0$ and $V_{sd} = 100$ mV. Charge lithography took place at $t \sim 6$ hours indicated by an arrow ($V_{write} = +10$ V). (b) Data from (a) expressed in terms of ΔV_{bg}. The $I(V_{bg})$ device characteristics were used to calculate the effective change in gate voltage ΔV_{bg}. The fit line is a double exponential decay with half lives of 1 and 14 hours.

The time evolution of ΔV_{bg} follows a bi-exponential decay (Fig. 5.8b). The bi-exponential behavior suggests that two mechanisms are causing ΔV_{bg} to decay. We hypothesize that the faster process corresponds to the build-up of screening charge in the SiO_2 near the CNT, while the slower process corresponds to the dissipation of λ_{litho} into the surrounding environment. Previous authors have verified that charge leaks from electrically connected CNTs into the nearby SiO_2 on a time scale of minutes to hours when radial electric fields are present.[4,18] This charge leaking effect leads to a build-up of charge that would screen the electric field generated by λ_{litho}. Compared to the process of charge leaking, the decay of λlitho should be significantly slower. The patterned charge is located far from any conducting objects so charge must migrate over the oxide surface, or through the oxide, to reach a conducting reservoir. We have used KFM imaging to confirm that λ_{litho} remains

localized on the oxide surface for several hours. Regardless of the exact decay mechanisms, the lifetime of the doping effect is long and provides ample time to explore the characteristics of a device with a tailored doping profile. Moreover, we expect that the mechanisms causing ΔV_{bg} to decay can be suppressed, if needed, by cooling the device to cryogenic temperatures.

5.5 Conclusion

In conclusion, we have used electrical characterization and scanning probe techniques to investigate the response of CNT FETs to lithographically patterned surface charge. The spatial resolution of the doping modulation is approximately 300 nm (the distance between the charge and CNT) and magnitude of ΔE_F is tunable up to ±1 eV. We have demonstrated a charge pattern that turns a CNT FET into a pn junction. Other simple charge patterns could be used to create devices such as double quantum dots, gradated p-i-n junctions, or FETs with engineered hotspots. We anticipate that the ability to controllably and reversibly modulate the doping profiles in nanoscale electronic and optoelectronic devices will enable a variety of new investigations.

5.6 Acknowledgements

References and Notes

1. Xia, F., Mueller, T., Lin, Y.-ming, Valdes-Garcia, A. & Avouris, P. Ultrafast graphene photodetector. *Nat Nano* **4**, 839-843 (2009).

2. Tersoff, J. Low-Frequency Noise in Nanoscale Ballistic Transistors. *Nano Letters* **7**, 194-198 (2007).

3. Lee, J.S. et al. Origin of Gate Hysteresis in Carbon Nanotube Field-Effect Transistors. *The Journal of Physical Chemistry C* **111**, 12504-12507 (2007).

4. Fuhrer, M.S., Kim, B.M., Dürkop, T. & Brintlinger, T. High-Mobility Nanotube Transistor Memory. *Nano Letters* **2**, 755-759 (2002).

5. Tans, S.J. & Dekker, C. Molecular transistors: Potential modulations along carbon nanotubes. *Nature* **404**, 834-835 (2000).

6. Freitag, M. et al. Scanning photovoltage microscopy of potential modulations in carbon nanotubes. *Appl. Phys. Lett.* **91**, 031101 (2007).

7. Crook, R. et al. Erasable electrostatic lithography for quantum components. *Nature* **424**, 751-754 (2003).

8. Valdrè, G. et al. Controlled positive and negative surface charge injection and erasure in a GaAs/AlGaAs based microdevice by scanning probe microscopy. *Nanotechnology* **19**, 045304 (2008).

9. Xie, Y., Bell, C., Yajima, T., Hikita, Y. & Hwang, H.Y. Charge Writing at the LaAlO3/SrTiO3 Surface. *Nano Letters* **10**, 2588-2591 (2010).

10. Tomiye, H. & Yao, T. Scanning capacitance microscope study of a SiO 2 /Si interface modified by charge injection. *Applied Physics A: Materials Science & Processing* **66**, S431-S434 (1998).

11. Brunel, D., Mayer, A. & Mélin, T. Imaging the Operation of a Carbon Nanotube Charge Sensor at the Nanoscale. *ACS Nano* **4**, 5978-5984 (2010).

12. Kong, J., Soh, H.T., Cassell, A.M., Quate, C.F. & Dai, H. Synthesis of individual single-walled carbon nanotubes on patterned silicon wafers. *Nature* **395**, 878-881 (1998).

13. Leng, Y. Molecular charge mapping with electrostatic force microscope. *Proceedings of SPIE* 35-39 (1993).doi:10.1117/12.146383

14. Park, J.-Y., Yaish, Y., Brink, M., Rosenblatt, S. & McEuen, P.L. Electrical cutting and nicking of carbon nanotubes using an atomic force microscope. *Appl. Phys. Lett.* **80**, 4446-4448 (2002).

15. Nonnenmacher, M., O'Boyle, M.P. & Wickramasinghe, H.K. Kelvin probe force microscopy. *Appl. Phys. Lett.* **58**, 2921 (1991).

16. Minot, E.D. et al. Tuning Carbon Nanotube Band Gaps with Strain. *Phys. Rev. Lett.* **90**, 156401 (2003).

17. Kim, W. et al. Hysteresis Caused by Water Molecules in Carbon Nanotube Field-Effect Transistors. *Nano Letters* **3**, 193-198 (2003).

18. Radosavljević, M., Freitag, M., Thadani, K.V. & Johnson, A.T. Nonvolatile Molecular Memory Elements Based on Ambipolar Nanotube Field Effect Transistors. *Nano Letters* **2**, 761-764 (2002).

CHAPTER 6

Summary

The main goals of this work were to utilize atomic force microscopy (AFM) based characterization and engineering techniques to produce state-of-the-art nanoscale electronic components, and to understand their operation principles and potential applications. The function of carbon nanotube (CNT) electronic devices was controlled through AFM charge lithography and through incorporation of point defects into the CNT sidewall. Transport through point defects was experimentally explored, and a model was developed to explain observations. A main thrust of the research was aimed toward single-molecule resolution with point-defect based CNT sensors. Single molecule resolution was demonstrated, and in a theoretical study we explored the potential use of point-defect based CNT devices to study enzymatic processes at the single-molecule level.

Often, the function of an electronic device is governed by the junction of two materials with different properties. Therefore, control over the function of a device may be achieved through control over the spatial doping profile along the length of the conduction channel. We used electrical characterization and scanning probe techniques to investigate the response of CNT field-effect transistors (FETs) to lithographically patterned surface charge. Written charge patterns spatially modulated the Fermi level in a nearby CNT. The spatial resolution of the doping modulation was approximately 300 nm and the magnitude of the Fermi level shift was tunable up to ± 1 eV. We demonstrated a charge pattern which reconfigured a CNT FET into a pn junction. Other patterns could produce quantum dots, gradated p-i-n junctions, or FETs with engineered hotspots. We anticipate that the ability to controllably and reversibly modulate the doping profiles in nanoscale electronic and optoelectronic devices will enable a variety of new investigations.

Another route to modify the electronic properties of a nanoscale device is through incorporation of defects. Semiconducting point defects were engineered into the CNT sidewall with voltage pulses from an AFM probe. A single engineered defect often dominates transport, and the formation of a localized electron bottleneck can be verified through AFM-based techniques. In these devices, the unmodified sections of the CNT serve only as contact electrodes to the atomic-sized transistor device. We have reviewed the 'tool box' of AFM-based techniques which researchers use to study and engineer

nanoelectronic devices. We used DC and AC electrostatic force microscopy to identify the locations and resistances of individual CNTs connected in parallel. Next, scanning gate microscopy (SGM) and tip modulated-SGM were used to reveal the semiconducting response of each CNT. With this information a single CNT with desirable properties was singled out from the network for further experimentation. The unwanted CNTs were electrically cut with a biased AFM probe to leave a device containing a single CNT. An atomic-sized transistor with chemical functionality was engineered in the remaining CNT using a voltage pulse from the AFM probe. This nanotransistor was then demonstrated as a single-molecule sensor to detect *N*-(3-Dimethylaminopropyl)-*N'*-ethylcarbodiimide in an aqueous environment.

It is essential to understand the properties of CNT point defects before next-generation sensors can be built. Electronic transport through defects is still not well understood, and it has remained a challenge to link theoretical and experimental studies. We have attempted to resolve some inconsistancies between theory and experiment relating to transport through CNT defects. We conclude that the AFM method of incorporating point defects in CNTs leads to a range of different defect types with distinct electrical characteristics. We developed a new model to explain the experimentally observed p-type behavior of CNT point defects. Our modeling of electron transport through a Coulomb barrier shows that the charge of the defect, which varies based on chemical structure, strongly influences electrical characteristics. Our measurements of resonant scattering and tunneling suggest that the spectrum of impurity state energy levels associated with a defect also strongly influences electrical characteristics.

Nanotransistor sensors offer a new approach to track single-molecule reactions. Particularly exciting is the use of these sensors to study enzymatic activity at the single-molecule level. Point-defect based CNT sensors could potentially be used as an electronic-based complement to existing optical-based single-molecule methods. We presented a theoretical study of point-defect based CNT devices as single-enzyme sensors. Our calculations show that the processes of substrate binding and internal dynamics of enzymes can be detected with a nanotransistor sensor. At physiological salt concentrations ([salt] ~ 100 mM), signals are below the limits of detection for existing

devices; therefore, we conclude that the general applicability of these sensors is currently limited to (i) studying enzymes that are active when salt concentrations are lower than physiological conditions and (ii) studying enzyme processes involving highly charged substrate molecules. Our modeling predicts a time resolution of ~1 μs, which is significantly faster than existing single-molecule techniques. We expect that application of our computational methods to more enzyme systems will reveal many biologically relevant single-molecule processes that are potentially detectable with nanotransistor detection schemes. Additional applications of these computational methods will include the prediction of signals from nanotransistor-based immunoassay sensors.

Future work will aim for greater control over the defect generation process and more detailed theory to match the chemical structure of a defect with its electron transport signature. Point-defect based CNT sensors are ready for single-enzyme studies, and proof-of-principle experiments are underway.

BIBLIOGRAPHY

Allen, B.L., Kichambare, P.D. & Star, A. Carbon Nanotube Field-Effect-Transistor-Based Biosensors. Advanced Materials 19, 1439-1451 (2007).

Ashraf, M.K., Bruque, N.A., Pandey, R.R., Collins, P.G. & Lake, R.K. Effect of localized oxygen functionalization on the conductance of metallic carbon nanotubes. Phys. Rev. B 79, (2009).

Bachtold, A. et al. Aharonov-Bohm oscillations in carbon nanotubes. Nature 397, 673-675 (1999).

Bachtold, A. et al. Scanned Probe Microscopy of Electronic Transport in Carbon Nanotubes. Phys. Rev. Lett. 84, 6082 (2000).

Baker, N.A., Sept, D., Joseph, S., Holst, M.J. & McCammon, J.A. Electrostatics of nanosystems: Application to microtubules and the ribosome. Proceedings of the National Academy of Sciences 98, 10037 -10041 (2001).

Ballauff, M. & Jusufi, A. Anomalous small-angle X-ray scattering: analyzing correlations and fluctuations in polyelectrolytes. Colloid Polym Sci 284, 1303-1311 (2006).

Banerjee, S. & Wong, S.S. Rational Sidewall Functionalization and Purification of Single-Walled Carbon Nanotubes by Solution-Phase Ozonolysis. The Journal of Physical Chemistry B 106, 12144-12151 (2002).

Becker, R.S., Golovchenko, J.A. & Swartzentruber, B.S. Atomic-scale surface modifications using a tunnelling microscope. Nature 325, 419-421 (1987).

Bell, J.A. et al. Comparison of the crystal structure of bacteriophage T4 lysozyme at low, medium, and high ionic strengths. Proteins: Structure, Function, and Bioinformatics 10, 10-21 (1991).

Berthe, M. et al. Reversible Defect Engineering of Single-Walled Carbon Nanotubes Using Scanning Tunneling Microscopy. Nano Letters 7, 3623-3627 (2007).

Besteman, K., Lee, J.-O., Wiertz, F.G.M., Heering, H.A. & Dekker, C. Enzyme-Coated Carbon Nanotubes as Single-Molecule Biosensors. Nano Letters 3, 727-730 (2003).

Binnig, G. & Rohrer, H. Scanning Tunneling Microscopy. Surface Science 126, 236-244 (1983).

Binnig, G., Quate, C.F. & Gerber, C. Atomic Force Microscope. Phys. Rev. Lett. 56, 930 (1986).

Binnig, G., Rohrer, H., Gerber, C. & Weibel, E. Tunneling through a controllable vacuum gap. Applied Physics Letters 40, 178 (1982).

Björk, M.T. et al. Nanowire resonant tunneling diodes. Applied Physics Letters 81, 4458 (2002).

Blank, K., De Cremer, G. & Hofkens, J. Fluorescence-based analysis of enzymes at the single-molecule level. Biotechnology Journal 4, 465-479 (2009).

Blank, K., Gert De Cremer & Johan Hofkens Fluorescence-based analysis of enzymes at the single-molecule level. Biotechnology Journal 4, 465-479 (2009).

Bockrath, M. et al. Luttinger-liquid behaviour in carbon nanotubes. Nature 397, 598-601 (1999).

Bockrath, M. et al. Single-Electron Transport in Ropes of Carbon Nanotubes. Science 275, 1922 -1925 (1997).

Brooks Shera, E., Seitzinger, N.K., Davis, L.M., Keller, R.A. & Soper, S.A. Detection of single fluorescent molecules. Chemical Physics Letters 174, 553-557 (1990).

Bruchez, M., Moronne, M., Gin, P., Weiss, S. & Alivisatos, A.P. Semiconductor Nanocrystals as Fluorescent Biological Labels. Science 281, 2013 -2016 (1998).

Brunel, D., Mayer, A. & Mélin, T. Imaging the Operation of a Carbon Nanotube Charge Sensor at the Nanoscale. ACS Nano 4, 5978-5984 (2010).

Buchs, G. et al. Creation of paired electron states in the gap of semiconducting carbon nanotubes by correlated hydrogen adsorption. New J. Phys. 9, 275-275 (2007).

Buchs, G., Ruffieux, P., Gröning, P. & Gröning, O. Defect-induced negative differential resistance in single-walled carbon nanotubes. Applied Physics Letters 93, 073115 (2008).

Buchs, G., Ruffieux, P., Gröning, P. & Gröning, O. Scanning tunneling microscopy investigations of hydrogen plasma-induced electron scattering centers on single-walled carbon nanotubes. Applied Physics Letters 90, 013104 (2007).

Carneiro, M.A., Venezuela, P. & Fagan, S.B. First Principles Calculations of Alanine Radicals Adsorbed on Pristine and Functionalized Carbon Nanotubes. The Journal of Physical Chemistry C 112, 14812-14815 (2008).

Chan, W.C.W. & Nie, S. Quantum Dot Bioconjugates for Ultrasensitive Nonisotopic Detection. Science 281, 2016 -2018 (1998).

Chen, Y., Hu, D., Vorpagel, E.R. & Lu, H.P. Probing Single-Molecule T4 Lysozyme Conformational Dynamics by Intramolecular Fluorescence Energy Transfer. The Journal of Physical Chemistry B 107, 7947-7956 (2003).

Choi, H.J., Ihm, J., Louie, S.G. & Cohen, M.L. Defects, Quasibound States, and Quantum Conductance in Metallic Carbon Nanotubes. Phys. Rev. Lett. 84, 2917 (2000).

Colvin, V.L., Schlamp, M.C. & Alivisatos, A.P. Light-emitting diodes made from cadmium selenide nanocrystals and a semiconducting polymer. Nature 370, 354-357 (1994).

Coroneus, J.G. et al. Mechanism-Guided Improvements to the Single Molecule Oxidation of Carbon Nanotube Sidewalls. ChemPhysChem 9, 1053-1056 (2008).

Crook, R. et al. Erasable electrostatic lithography for quantum components. Nature 424, 751-754 (2003).

Cui, Y. & Lieber, C.M. Functional Nanoscale Electronic Devices Assembled Using Silicon Nanowire Building Blocks. Science 291, 851 -853 (2001).

da Silva, L.B., Fagan, S.B. & Mota, R. Carboxylated Carbon Nanotubes under External Electrical Field: An Ab Initio Investigation. The Journal of Physical Chemistry C 113, 8959-8963 (2009).

Das, R. et al. Counterion Distribution around DNA Probed by Solution X-Ray Scattering. Phys. Rev. Lett. 90, 188103 (2003).

Dixon, M.M., Nicholson, H., Shewchuk, L., Baase, W.A. & Matthews, B.W. Structure of a hinge-bending bacteriophage T4 lysozyme mutant, Ile3 --> Pro. Journal of Molecular Biology 227, 917-933 (1992).

Dolinsky, T.J. et al. PDB2PQR: expanding and upgrading automated preparation of biomolecular structures for molecular simulations. Nucleic Acids Research 35, W522-W525 (2007).

Dolinsky, T.J., Nielsen, J.E., McCammon, J.A. & Baker, N.A. PDB2PQR: an automated pipeline for the setup of Poisson-Boltzmann electrostatics calculations. Nucleic Acids Research 32, W665-W667 (2004).

English, B.P. et al. Ever-fluctuating single enzyme molecules: Michaelis-Menten equation revisited. Nat Chem Biol 2, 87-94 (2006).

Freitag, M. et al. Scanning photovoltage microscopy of potential modulations in carbon nanotubes. Appl. Phys. Lett. 91, 031101 (2007).

Fuhrer, M.S., Kim, B.M., Dürkop, T. & Brintlinger, T. High-Mobility Nanotube Transistor Memory. Nano Letters 2, 755-759 (2002).

Gabor, N.M. et al. Hot Carrier-Assisted Intrinsic Photoresponse in Graphene. arXiv:1108.3826 (2011).at <http://arxiv.org/abs/1108.3826>

Gabor, N.M., Zhong, Z., Bosnick, K., Park, J. & McEuen, P.L. Extremely Efficient Multiple Electron-Hole Pair Generation in Carbon Nanotube Photodiodes. Science 325, 1367 -1371 (2009).

Gao, X., Cui, Y., Levenson, R.M., Chung, L.W.K. & Nie, S. In vivo cancer targeting and imaging with semiconductor quantum dots. Nat. Biotechnol 22, 969-976 (2004).

Gibson, G.A., Smyth, J.F., Schultz, S. & Kern, D.P. Observation of the switching fields of individual Permalloyparticles in nanolithographic arrays via magnetic force microscopy. IEEE Transactions on Magnetics 27, 5187-5189 (1991).

Goldsmith, B.R. et al. Conductance-Controlled Point Functionalization of Single-Walled Carbon Nanotubes. Science 315, 77-81 (2007).

Goldsmith, B.R., Coroneus, J.G., Kane, A.A., Weiss, G.A. & Collins, P.G. Monitoring Single-Molecule Reactivity on a Carbon Nanotube. Nano Letters 8, 189-194 (2008).

Gruverman, A. Scanning force microscopy for the study of domain structure in ferroelectric thin films. Journal of Vacuum Science & Technology B: Microelectronics and Nanometer Structures 14, 602 (1996).

Henzler-Wildman, K.A. et al. Intrinsic motions along an enzymatic reaction trajectory. Nature 450, 838-844 (2007).

Hou, P.-X., Liu, C. & Cheng, H.-M. Purification of carbon nanotubes. Carbon 46, 2003-2025 (2008).

Iijima, S. Helical microtubules of graphitic carbon. Nature 354, 56-58 (1991).

Jalilian, R. et al. Scanning gate microscopy on graphene: charge inhomogeneity and extrinsic doping. Nanotechnology 22, 295705 (2011).

Javey, A. & Kong, J. Carbon Nanotube Electronics. (Springer: 2009).

Junno, T. et al. Single-electron devices via controlled assembly of designed nanoparticles. Microelectronic Engineering 47, 179-183 (1999).

Junno, T., Deppert, K., Montelius, L. & Samuelson, L. Controlled manipulation of nanoparticles with an atomic force microscope. Applied Physics Letters 66, 3627 (1995).

Kanai, Y., Khalap, V.R., Collins, P.G. & Grossman, J.C. Atomistic Oxidation Mechanism of a Carbon Nanotube in Nitric Acid. Phys. Rev. Lett. 104, 066401 (2010).

Keyser, U.F. et al. Direct force measurements on DNA in a solid-state nanopore. Nat Phys 2, 473-477 (2006).

Kim, D.-H., Koo, J.-Y. & Kim, J.-J. Cutting of multiwalled carbon nanotubes by a negative voltage tip of an atomic force microscope: A possible mechanism. Phys. Rev. B 68, 113406 (2003).

Kim, D.-H., Koo, J.-Y. & Kim, J.-J. Cutting of multiwalled carbon nanotubes by a negative voltage tip of an atomic force microscope: A possible mechanism. Phys. Rev. B 68, 113406 (2003).

Kim, H. et al. Local electronic density of states of a semiconducting carbon nanotube interface. Phys. Rev. B 71, 235402 (2005).

Kim, K.S. et al. Large-scale pattern growth of graphene films for stretchable transparent electrodes. Nature 457, 706-710 (2009).

Kim, W. et al. Hysteresis Caused by Water Molecules in Carbon Nanotube Field-Effect Transistors. Nano Letters 3, 193-198 (2003).

Kong, J., Soh, H.T., Cassell, A.M., Quate, C.F. & Dai, H. Synthesis of individual single-walled carbon nanotubes on patterned silicon wafers. Nature 395, 878-881 (1998).

Kundu, S., Wang, Y., Xia, W. & Muhler, M. Thermal Stability and Reducibility of Oxygen-Containing Functional Groups on Multiwalled Carbon Nanotube Surfaces: A Quantitative High-Resolution XPS and TPD/TPR Study. The Journal of Physical Chemistry C 112, 16869-16878 (2008).

Lahm, A. & Suck, D. DNase I-induced DNA conformation : 2 Å Structure of a DNase I-octamer complex. Journal of Molecular Biology 222, 645-667 (1991).

Lee, J.S. et al. Origin of Gate Hysteresis in Carbon Nanotube Field-Effect Transistors. The Journal of Physical Chemistry C 111, 12504-12507 (2007).

Lee, J.U. Photovoltaic effect in ideal carbon nanotube diodes. Appl. Phys. Lett. 87, 073101 (2005).

Lee, S. et al. Paired Gap States in a Semiconducting Carbon Nanotube: Deep and Shallow Levels. Phys. Rev. Lett. 95, 166402 (2005).

Lei, C.H., Das, A., Elliott, M. & Macdonald, J.E. Quantitative electrostatic force microscopy-phase measurements. Nanotechnology 15, 627-634 (2004).

Leng, Y. Molecular charge mapping with electrostatic force microscope. Proceedings of SPIE 35-39 (1993).doi:10.1117/12.146383

Li, J. et al. Carbon Nanotube Sensors for Gas and Organic Vapor Detection. Nano Letters 3, 929-933 (2003).

Liu, F. et al. Giant random telegraph signals in the carbon nanotubes as a single defect probe. Appl. Phys. Lett. 86, 163102 (2005).

Liu, Z., Sun, X., Nakayama-Ratchford, N. & Dai, H. Supramolecular Chemistry on Water-Soluble Carbon Nanotubes for Drug Loading and Delivery. ACS Nano 1, 50-56 (2007).

Manning, G.S. The Molecular Theory of Polyelectrolyte Solutions with Applications to the Electrostatic Properties of Polynucleotides. Quarterly Reviews of Biophysics 11, 179-246 (1978).

Martin, Y., Abraham, D.W. & Wickramasinghe, H.K. High-resolution capacitance measurement and potentiometry by force microscopy. Applied Physics Letters 52, 1103 (1988).

Mawhinney, D.B. et al. Infrared Spectral Evidence for the Etching of Carbon Nanotubes: Ozone Oxidation at 298 K. Journal of the American Chemical Society 122, 2383-2384 (2000).

Minot, E.D. et al. Tuning Carbon Nanotube Band Gaps with Strain. Phys. Rev. Lett. 90, 156401 (2003).

Miyata, Y., Maniwa, Y. & Kataura, H. Selective Oxidation of Semiconducting Single-Wall Carbon Nanotubes by Hydrogen Peroxide. The Journal of Physical Chemistry B 110, 25-29 (2006).

Nonnenmacher, M., O'Boyle, M.P. & Wickramasinghe, H.K. Kelvin probe force microscopy. Appl. Phys. Lett. 58, 2921 (1991).

Pan, Z.W. et al. Very long carbon nanotubes. Nature 394, 631-632 (1998).

Park, J. et al. Coulomb blockade and the Kondo effect in single-atom transistors. Nature 417, 722-725 (2002).

Park, J.-Y. Electrically tunable defects in metallic single-walled carbon nanotubes. Appl. Phys. Lett. 90, 023112-3 (2007).

Park, J.-Y., Yaish, Y., Brink, M., Rosenblatt, S. & McEuen, P.L. Electrical cutting and nicking of carbon nanotubes using an atomic force microscope. Appl. Phys. Lett. 80, 4446-4448 (2002).

Parkin, S.S.P., Hayashi, M. & Thomas, L. Magnetic Domain-Wall Racetrack Memory. Science 320, 190 -194 (2008).

Patolsky, F. et al. Electrical detection of single viruses. Proceedings of the National Academy of Sciences of the United States of America 101, 14017 -14022 (2004).

Peng, Y. & Liu, H. Effects of Oxidation by Hydrogen Peroxide on the Structures of Multiwalled Carbon Nanotubes. Industrial & Engineering Chemistry Research 45, 6483-6488 (2006).

Postma, H.W.C., Teepen, T., Yao, Z., Grifoni, M. & Dekker, C. Carbon Nanotube Single-Electron Transistors at Room Temperature. Science 293, 76 -79 (2001).

Prisbrey, L., DeBorde, T., Park, J.-Y. & Minot, E.D. Controlling the function of carbon nanotube devices with re-writable charge patterns. Appl. Phys. Lett. 99, 053125 (2011).

Prisbrey, L., Park, J.-Y., Blank, K., Moshar, A. & Minot, E.D. Scanning probe techniques to engineer nanoelectronic devices. Microscopy and Analysis (2012).

Prisbrey, L., Schneider, G. & Minot, E. Modeling the Electrostatic Signature of Single Enzyme Activity. The Journal of Physical Chemistry B 114, 3330-3333 (2010).

Priyadarshini, S. & Kansal, V.K. Biochemical Characterization of Buffalo (Bubalus Bubalis) Milk Lysozyme. Journal of Dairy Research 70, 467-471 (2003).

Radosavljević, M., Freitag, M., Thadani, K.V. & Johnson, A.T. Nonvolatile Molecular Memory Elements Based on Ambipolar Nanotube Field Effect Transistors. Nano Letters 2, 761-764 (2002).

Robinson, J.A., Snow, E.S., Bădescu, Ș.C., Reinecke, T.L. & Perkins, F.K. Role of Defects in Single-Walled Carbon Nanotube Chemical Sensors. Nano Letters 6, 1747-1751 (2006).

Rocha, A.R., Padilha, J.E., Fazzio, A. & da Silva, A.J.R. Transport properties of single vacancies in nanotubes. Phys. Rev. B 77, 153406 (2008).

Roschier, L. et al. Single-electron transistor made of multiwalled carbon nanotube using scanning probe manipulation. Applied Physics Letters 75, 728 (1999).

Rothberg, J.M. et al. An integrated semiconductor device enabling non-optical genome sequencing. Nature 475, 348-352 (2011).

Sorgenfrei, S. et al. Label-free single-molecule detection of DNA-hybridization kinetics with a carbon nanotube field-effect transistor. Nat Nano 6, 126-132 (2011).

Tans, S.J. & Dekker, C. Molecular transistors: Potential modulations along carbon nanotubes. Nature 404, 834-835 (2000).

Tans, S.J. et al. Individual single-wall carbon nanotubes as quantum wires. Nature 386, 474-477 (1997).

Tans, S.J., Verschueren, A.R.M. & Dekker, C. Room-temperature transistor based on a single carbon nanotube. Nature 393, 49-52 (1998).

Tersoff, J. Low-Frequency Noise in Nanoscale Ballistic Transistors. Nano Letters 7, 194-198 (2007).

Tolvanen, A. et al. Modifying the electronic structure of semiconducting single-walled carbon nanotubes by Ar+ ion irradiation. Phys. Rev. B 79, 125430 (2009).

Tomiye, H. & Yao, T. Scanning capacitance microscope study of a SiO 2 /Si interface modified by charge injection. Applied Physics A: Materials Science & Processing 66, S431-S434 (1998).

Valdrè, G. et al. Controlled positive and negative surface charge injection and erasure in a GaAs/AlGaAs based microdevice by scanning probe microscopy. Nanotechnology 19, 045304 (2008).

Veloso, M.V., Souza Filho, A.G., Mendes Filho, J., Fagan, S.B. & Mota, R. Ab initio study of covalently functionalized carbon nanotubes. Chemical Physics Letters 430, 71-74 (2006).

Warshel, A., Sharma, P.K., Kato, M. & Parson, W.W. Modeling electrostatic effects in proteins. Biochimica et Biophysica Acta (BBA) - Proteins & Proteomics 1764, 1647-1676 (2006).

Wepasnick, K.A., Smith, B.A., Bitter, J.L. & Howard Fairbrother, D. Chemical and structural characterization of carbon nanotube surfaces. Anal Bioanal Chem 396, 1003-1014 (2010).

Wilson, N.R. & Cobden, D.H. Tip-Modulation Scanned Gate Microscopy. Nano Letters 8, 2161-2165 (2008).

Xia, F., Mueller, T., Lin, Y.-ming, Valdes-Garcia, A. & Avouris, P. Ultrafast graphene photodetector. Nat Nano 4, 839-843 (2009).

Xie, Y., Bell, C., Yajima, T., Hikita, Y. & Hwang, H.Y. Charge Writing at the LaAlO3/SrTiO3 Surface. Nano Letters 10, 2588-2591 (2010).

Yan, M. & Bernstein, G.H. A quantitative method for dual-pass electrostatic force microscopy phase measurements. Surface and Interface Analysis 39, 354-358 (2007).

Yu, M.-F. et al. Strength and Breaking Mechanism of Multiwalled Carbon Nanotubes Under Tensile Load. Science 287, 637 -640 (2000).

Zhang, X.-jun, Wozniak, J.A. & Matthews, B.W. Protein Flexibility and Adaptability Seen in 25 Crystal Forms of T4 Lysozyme. Journal of Molecular Biology 250, 527-552 (1995).

Zhang, Y., Tan, Y.-W., Stormer, H.L. & Kim, P. Experimental observation of the quantum Hall effect and Berry's phase in graphene. Nature 438, 201-204 (2005).

Zhao, J. et al. Engineering the Electronic Structure of Single-Walled Carbon Nanotubes by Chemical Functionalization. ChemPhysChem 6, 598-601 (2005).

Zhao, J., Park, H., Han, J. & Lu, J.P. Electronic Properties of Carbon Nanotubes with Covalent Sidewall Functionalization. The Journal of Physical Chemistry B 108, 4227-4230 (2004).

Zheng, G., Gao, X.P.A. & Lieber, C.M. Frequency Domain Detection of Biomolecules Using Silicon Nanowire Biosensors. Nano Letters 10, 3179-3183 (2010).

Zheng, G., Patolsky, F., Cui, Y., Wang, W.U. & Lieber, C.M. Multiplexed electrical detection of cancer markers with nanowire sensor arrays. Nat Biotech 23, 1294-1301 (2005).

Zhou, X., Dayeh, S.A., Wang, D. & Yu, E.T. Scanning gate microscopy of InAs nanowires. Applied Physics Letters 90, 233118 (2007).